

The Effect of Soil Structure Interaction on the Behavior of Base Isolated Structures

by

Boya Yin

Department of Civil and Environmental Engineering  
Duke University

Date: \_\_\_\_\_

Approved:

\_\_\_\_\_  
Henri P. Gavin, Supervisor

\_\_\_\_\_  
Lawrence N. Virgin

\_\_\_\_\_  
Fred K. Boadu

\_\_\_\_\_  
Tomasz Hueckel

Thesis submitted in partial fulfillment of  
the requirements for the degree of  
Master of Science in the Department of  
Civil and Environmental Engineering in the Graduate School of  
Duke University

2014

ABSTRACT

The Effect of Soil Structure Interaction on the Behavior of Base Isolated Structures

by

Boya Yin

Department of Civil and Environmental Engineering  
Duke University

Date: \_\_\_\_\_

Approved:

\_\_\_\_\_  
Henri P. Gavin, Supervisor

\_\_\_\_\_  
Lawrence N. Virgin

\_\_\_\_\_  
Fred K. Boadu

\_\_\_\_\_  
Tomasz Hueckel

An abstract of a thesis submitted in partial  
fulfillment of the requirements for the degree  
of Master of Science in the Department of  
Civil and Environmental Engineering in the Graduate School of  
Duke University

2014

Copyright by  
Boya Yin  
2014

## **Abstract**

This master thesis investigates the effect of soil structure interaction on the behavior of base isolated structures. A linear soil model coupled with a nonlinear model of a base-isolated structure is assembled as a nonlinear system in state-space. Transient responses to earthquake ground motions are computed by integrating the nonlinear equations with a fixed-time step. Earthquake ground motions representative of near-fault and far-field conditions are generated and tested for this system. The effects of soil compliance and friction in the base isolation system are then evaluated. An eigenvalue analysis of the dynamics matrix of the couple system gives the evidence that the soil structure interaction increases the periods of the structure positively. It is shown that the base isolation system with large hysteretic frictional force is less effective in achieving the goals of seismic isolation; large isolation-level friction couples the structure above it too tightly, which results in less deformation in base isolator and larger roof acceleration than intended for a seismically-isolated structure. In addition, the base isolation system with large hysteretic frictional force produces larger residual displacements for both base isolator and the above floors. The impact factor of shear wave velocity to the stiffness of soil is more difficult to assess. Therefore, nonlinear liquefied soil model is recommended to be calibrated for soil structure interaction evaluation as well as to be

compared with empirical testing. To this end, nonlinear models for liquefying soil are investigated.

# Contents

Abstract .....	iv
List of Tables.....	viii
List of Figures .....	ix
Acknowledgements .....	xii
1. Introduction .....	1
1.1 General Remarks .....	1
1.2 Objectives and Scope.....	2
1.3 Organization of the Thesis .....	3
2. Literature Review.....	4
2.1 Constitutive Models used in Soil Liquefaction Problem .....	4
2.2 Soil Structure Interaction.....	8
2.3 Seismic Isolation .....	10
3. Linear Soil Modeling and Interactions.....	14
3.1 Notation .....	14
3.2 Construction of Cone Model.....	16
3.3 Equations of Motion.....	18
3.3.1 Soil-Foundation .....	18
3.3.2 Superstructure.....	19
3.4 State Space .....	21
3.5 Numerical Procedure with MATLAB.....	23

3.5.1 Example 1: 100 m/s shear wave velocity, low frictional force.....	24
3.5.2 Example 2: 200 m/s shear wave velocity, low frictional force.....	30
3.5.3 Example 3: 200 m/s shear wave velocity, high frictional force .....	35
3.6 Discussion.....	40
4. Parameter Analysis.....	44
4.1 Numerical Examples.....	44
4.1.1 Example 1: Synthetic far field earthquake ground motion .....	45
4.1.2 Example 2: Synthetic near field without pulse earthquake ground motion .....	52
4.1.3 Example 3: Synthetic near field with pulse earthquake ground motion .....	57
4.2 Discussion.....	62
5. Nonlinear Soil Modeling.....	64
5.1 Cubrinovski's soil model.....	65
5.2 2D plasticity formulation.....	70
6. OpenSees Simulation.....	75
6.1 UCSD Soil Model.....	76
6.2 Discussion.....	81
7. Conclusions.....	82
References .....	83

## List of Tables

Table 1: Parameters used to design the whole system. ....	24
Table 2: Natural frequency and damping factor for soil-foundation system (Example 1). .....	26
Table 3: Natural frequency and damping factor for superstructure system (Example 1).	26
Table 4: Natural frequency and damping factor for the whole system (Example 1). ....	26
Table 5: Natural frequency and damping factor for soil-foundation system (Example 2). .....	31
Table 6: Natural frequency and damping factor for superstructure system (Example 2).	31
Table 7: Natural frequency and damping factor for the whole system (Example 2). ....	32
Table 8: Natural frequency and damping factor for soil-foundation system (Example 3). .....	36
Table 9: Natural frequency and damping factor for superstructure system (Example 3).	36
Table 10: Natural frequency and damping factor for the whole system (Example 3). ....	36
Table 11: Parameters values for earthquake ground motions .....	41

## List of Figures

Figure 1: Physical model of the foundation system. ....	16
Figure 2: Dimension of foundation.....	17
Figure 3: Visual representation of 1-D model. ....	19
Figure 4: Artificial far field ground motion record (Example 1). ....	27
Figure 5: Displacement and velocity response for soil and each floor (Example 1). ....	28
Figure 6: Two rocking degrees of freedom response (Example 1). ....	28
Figure 7: Hysteresis loop (Example 1). ....	29
Figure 8: Base isolator deformation, roof acceleration, and base shear ratio ....	29
Figure 9: Artificial far field ground motion record (Example 2). ....	32
Figure 10: Displacement and velocity response for soil and each floor (Example 2). ....	33
Figure 11: Two rocking degrees of freedom response (Example 2). ....	33
Figure 12: Hysteresis loop (Example 2). ....	34
Figure 13: Base isolator deformation, roof acceleration, and base shear ratio. (Example 2) .....	35
Figure 14: Artificial far field ground motion record (Example 3). ....	37
Figure 15: Displacement and velocity response for soil and each floor (Example 3). ....	38
Figure 16: Two rocking degrees of freedom response (Example 3). ....	38
Figure 17: Hysteresis loop (Example 3). ....	39
Figure 18: Base isolator deformation, roof acceleration, and base shear ratio. (Example 3) .....	40
Figure 19: Peak isolator deformation vs. Frictional force (FF). ....	48

Figure 20: Peak roof acceleration vs. Frictional force (FF).....	48
Figure 21: Base shear vs. Frictional force (FF).....	49
Figure 22: Peak isolator deformation empirical C.D.F (FF). ....	49
Figure 23: Peak roof acceleration empirical C.D.F (FF). ....	50
Figure 24: Peak normalized base shear empirical C.D.F (FF). ....	50
Figure 25: Peak isolator deformation empirical P.D.F, 6000 simulations (FF). ....	51
Figure 26: Residual base isolator deformation (FF).....	51
Figure 27: Peak isolator deformation vs. Frictional force (NFNP).....	53
Figure 28: Peak roof acceleration vs. Frictional force (NFNP).....	53
Figure 29: Base shear vs. Frictional force (NFNP).....	54
Figure 30: Peak isolator deformation empirical C.D.F (NFNP).....	54
Figure 31: Peak roof acceleration empirical C.D.F (NFNP). ....	55
Figure 32: Peak normalized base shear empirical C.D.F (NFNP). ....	55
Figure 33: Peak isolator deformation empirical P.D.F, 6000 simulations (NFNP).....	56
Figure 34: Residual base isolator deformation (NFNP).....	56
Figure 35: Peak isolator deformation vs. Frictional force (NFP). ....	58
Figure 36: Peak roof acceleration vs. Frictional force (NFP). ....	58
Figure 37: Base shear vs. Frictional force (NFP). ....	59
Figure 38: Peak base isolator deformation empirical C.D.F (NFP). ....	59
Figure 39: Peak roof acceleration empirical C.D.F (NFP).....	60
Figure 40: Peak normalized base shear empirical C.D.F (NFP).....	60
Figure 41: Peak isolator deformation empirical P.D.F, 6000 simulations (NFP).....	61

Figure 42: Residual base isolator deformation (NFP).....	61
Figure 43: Definition of state index $I_s$ (Ishihara 1993).....	66
Figure 44: Degradation of normalized initial shear modulus vs. shear strain (Cubrinovski and Ishihara 1998).....	68
Figure 45: Flow rule (Gutierrez et al., 1993). ....	72
Figure 46: Size of loading surface and failure surface (Cubrinovski and Ishihara 1998). ....	73
Figure 47: Lateral displacement for soil element at different depth.....	78
Figure 48: Lateral acceleration for soil element at different depth. ....	78
Figure 49: Stress-strain output at 2 m depth. ....	79
Figure 50: Stress-strain output at 6 m depth. ....	79
Figure 51: Stress-strain output at 10 m depth. ....	80
Figure 52: Excess pore water pressure for soil element at different depth. ....	80

## **Acknowledgements**

I would like to express my deepest gratitude to my advisor, Dr. Henri Gavin, for his excellent guidance, generous caring and patience, and for providing me with an excellent atmosphere for doing research. I couldn't finish this thesis without his generous help.

I would like to express enough thanks to my committee, Dr. Lawrence Virgin, Dr. Fred Boadu, Dr. Tomasz Hueckel, who are willing to attend my thesis defense.

I would like to thank my excellent parents, who are always supporting me and encouraging me with their best wishes.

Finally, I would like to thank my husband, Zhang Ying. He is always there standing by me no matter good time or bad time.

# 1. Introduction

## 1.1 General Remarks

Soil liquefaction causes severe damage to structures and is one of the most complicated phenomena during earthquakes. It is likely to occur in saturated, loose sandy soil because loose sandy soil has a tendency to consolidate under an applied load. When loose sandy soil is saturated with water, and loaded dynamically, the normal stress can be transferred from the soil skeleton to the pore water due to rapid volumetric strain and limited hydraulic conductivity of the soil. If the hydraulic conductivity is low, the accumulated pore water pressure is not rapidly dissipated during the seismic shaking, resulting in an increase of pore water pressure. The increase of pore water pressure reduces the shear strength and the stiffness. What's more, the liquefaction-related damage mostly results from a reduction in effective confining stress and the associated loss of strength and stiffness (Idriss 2008). The loss of strength of the soil skeleton implies that the soil skeleton loses the ability to transfer shear stress. The soil then behaves like a liquid. Structures supported by liquefying soils may be severely damaged or even collapse.

In order to mitigate the liquefaction of soil due to earthquakes, two main philosophies can be summarized based on decades of researches. One is to prevent the generation of excess pore water pressure, the other is to reduce the liquefaction-associated deformations of the soil (Idriss 2008). In recent years, especially in developed

countries, engineers are required to consider the effects of soil liquefaction in the design of new infrastructures like buildings, bridges, dams, tunnels and other retaining structures (NEHRP 2004). In the last two decades, the effects of soil liquefaction have been thoroughly brought to attention and many studies related to this field have been proposed (UC Davis NEES Center for Geotechnical Modeling, Center for Earthquake Engineering Simulation).

## **1.2 Objectives and Scope**

This project is conducted in order to better understand the nonlinear liquefied soil behaviors, base-isolated structure system as well as their interactions under earthquake ground motions. Primarily, a linearized soil model based on Wolf's soil model (Wolf 1994) is to be calibrated and coupled with a base-isolated structure. Then the model is implemented in MATLAB and a parameter analysis is conducted through several simulation examinations. The relationships and trends between the system response and the system parameters are investigated. The behavior of base isolation system is then evaluated by examining the deformation of the isolation system and the deformation of the super-structure. Additionally, characteristics of the selected nonlinear stress-strain-dilatancy model (Cubrinovski and Ishihara 1998) is discussed and simulation using the OpenSees numerical platform is introduced.

(<http://opensees.berkeley.edu/>)

### **1.3 Organization of the Thesis**

Chapter 1 introduces the background and motivation of this thesis. The objectives and scope are also described in Chapter 1. The organization of the thesis is outlined in Chapter 1 as well. Chapter 2 gives a literature review about the key concepts that are concerned in this project, including the constitutive models used in simulating soil liquefaction, soil-structure interaction and seismic isolation. Chapter 3 describes a linear soil modeling and its interactions with the foundation and superstructure of a nonlinear structure. A comprehensive process of modeling including the derivation of equations for each component of the system, assembly of equations to a coupled system, putting the equations into state space form, accompanied by numerical implementation in MATLAB is illustrated in Chapter 3. Chapter 4 discusses a parameter analysis for the same soil-structure system, however, with three different synthesized earthquake ground motions. The results of 18000 simulations are discussed and the behaviors of the base isolation system are evaluated. Chapter 5 extends to nonlinear soil models, describes the features and the advantages of using a state-variable nonlinear soil model (Cubrinovski and Ishihara 1998). Chapter 6 discusses a currently used UCSD soil model and its implementation in OpenSees. Chapter 7 discusses some conclusions accomplished in this project and offers some recommendations for future work.

## **2. Literature Review**

In this chapter, a literature review is conducted on the constitutive models commonly used in soil liquefaction problem, soil-foundation-structure interactions, and seismic isolation concepts.

### **2.1 Constitutive Models used in Soil Liquefaction Problem**

Why does loose sandy soil have a characteristic of contractility? Due to the incompressibility of the soil particles, two competing mechanisms, sliding and rolling determine the deformation of the soil. In loose sandy soil, sliding dominates and induces shear and contractive volumetric strains through the rearranging the soil particles to a denser skeleton. Not only the soil density, but also the ratio of deviatoric to hydrostatic stress influences the domination of various mechanisms (Dafalias 1994). Therefore, it is important to consider the combined effects of sand density and the stress ratio. On the contrary, rolling induces shear and dilatancy which is a main characteristic of dense sand.

In recent decades, three types of constitutive models have been used in concerning soil liquefaction problems. These constitutive models have been developed to effectively describe the hysteretic nonlinear and irreversible behavior of soil.

The first group includes elasto-plastic models (Zienkiewicz and Chang 1978, Jefferies 1993, Zienkiewicz and Chang 1978 and et al.). The most pronounced feature of these models is that stresses and corresponding strains are computed in increments. In

other words, both monotonic and cyclic stress paths are obtained through integration of the incremental relations.

Classical plasticity models belong to elasto-plastic models. The traditional characteristics of classical plasticity models can satisfy the need of simulating the response under cyclic loading conditions, however, sometimes it doesn't work well (Jefferies 1993).

Zienkiewicz and Chang (1978) proposed a simple plasticity model using a Mohr-Coulomb yield criterion and non-associative flow rule. Jefferies (1993) developed a classical isotropic plasticity model within the framework of critical state soil mechanics from the point view of general formulation, with associative flow rule, isotropic hardening and critical state concept characteristics.

Generalized plasticity models are based on a generalized plasticity formulation proposed by Zienkiewicz and Mroz (1984) from the point of view that the plastic modulus depends on a stress-ratio distance between the failure and the current stress ratio.

Within elasto-plastic models, bounding surface models were developed by Dafalias (1968). The remarkable feature of various versions of this type of model is that for the stress points which haven't reached the bounding surface, the distance between the actual stress and the image stress on the surface, accompanied by the plastic modulus determine the position of plastic yielding. Yogachandran (1991) developed a

bounding surface model in which two ellipses are used for the shape of bounding surface in first and second deviatoric stress-invariants space. Wang, Dafalias and Shen (1990) developed a hypo-plastic model stating that the strain-rate direction depends on the stress-rate direction based on the concept of a vanishing elastic region. Ishihara and Cubrinovski (1998) relate the values of model parameters by empirical relations to physically meaningful quantities such as stress and state index. When implemented numerically, it is convenient to consider a conical yield surface and a plastic potential surface during unloading and to use an associative flow rule for both loading and unloading stages. Proubet (1991) used a phase transformation line intersecting the failure line. The location of the intersection point depends on the density.

Another version of elasto-plastic models is the Nested-surfaces model proposed by Mroz (1967) and Iwan (1967). Nested-surfaces models consider a set of surfaces in stress space and locate the trajectory of constant plastic modulus. The kinematic hardening occurs at the active surface where the stress points are related to the pre-described plastic modulus in the plastic loading process, until the next surface is reached and becomes the active surface. Prevost (1985) proposed conical nested yield surfaces. Lacy(1986) developed two additional yield surfaces in the form of deviatoric planes in stress space, perpendicular to the hydrostatic stress axis, effectively capping the conical yield surfaces from two sides.

The second group includes micromechanical and multi-mechanism models (Matsuoka and Sakakibara 1987, Aubry, et al. 1982, Pande and Sharma 1983, Iai 1993). These models have the feature that the overall response is obtained by superposing the response of smaller units. These models also integrate the incremental relations to get monotonic and cyclic stress path.

The third group includes partially coupled or uncoupled models (Bouckovalas, et al. 1991, Finn, et al. 1977, Seed 1979, Towhata, et al. 1992). These models don't necessarily provide tensorial incremental stress-strain relation for all components. The analytic relations based on experience and observations are established between quantities of direct interest to the problem of liquefaction. Whether or not the geometrical or loading conditions are satisfied determine the validity of these models. The models still need to be modified to account for nonlinear soil behavior and to provide realistic simulations.

In this thesis, Cubrinovski and Ishihara's modified elasto-plasticity model is used to model the monotonic and cyclic behavior of liquefied soil because of several distinctive advantages.

Large amount of experimental data for soils are typically not available. It is expected that fewer parameter values can be effectively used in the model. In Cubrinovski and Ishihara's model, only a single set of material parameters is needed in

modeling sand behavior through the integration of state concept and the modified elasto-plasticity framework.

Another distinctive feature of this model is that the stress-strain-dilatancy model is incorporated into the elasto-plastic framework which makes the model more applicable to more general loading situations.

In addition, a finite element application for liquefied soil is currently being implemented in OpenSees based on Cubrinovski and Ishihara's modified elasto-plasticity model.

## **2.2 Soil Structure Interaction**

Soil structure interaction (SSI) describes the interaction between dynamic ground motion and structural motion. When a volume of soft soil is shaken by bed-rock motions, the deformation of the ground and the structures are not independent of each other. For systems with significant soil-structure interaction, the ground motion affects the response of structures and the motion of structures affects the response of the ground. Soil structure interaction involves two mechanisms, (1) kinematic interaction and (2) inertial interaction. The "free-field" is the space far enough from any foundation that the ground motion (called free-field ground motion) is not affected by the motion of nearby structures. In general, foundation motions do not match the free field ground motion at wave lengths that are shorter than the foundation dimensions. This effect is termed kinematic interaction. On the other hand, the structure has a large mass and

transmits inertial forces to the soil which induces soil deformations. This phenomenon is termed as inertial interaction (Wolf 1985).

Conventionally, soil structure interaction effects could be reasonably neglected in the simplified design for light structures with low rise built on stiff soil. However, for high rise building or building built on soft soil, the effect of soil structure interaction cannot be neglected. The National Earthquake Hazard Reduction Program classifies soil stiffness according to the soil shear wave velocity. Stiff soils are classified as having a shear wave velocity at a depth of 10 meters above 760 m/s. Soft soils have a shear wave velocity below 360 m/s (BSSC 2003).

An analysis of soil structure interaction effects on instrumented building was conducted (Zaicenco and Alkaz 2007, Zaicenco and Alkaz 2008). The observed data of the structural response in comparison with finite element analysis clearly give the evidence that soil structure interaction makes the system more flexible and increases the natural period of the structure. Moreover, SSI reduces the high frequency of the foundation motion, as compared to the soil motion. Based on certain rigorous numerical analysis (Mylonakis and Gazetas 2000), it is shown that the period of seismic waves are largely elongated in soft soils and thus may lead to the resonance of the structure with the ground motion. This resonance may cause hazardous large deformations of the structure and the soil. In addition, the foundation damping incorporates the effects of energy dissipation in the soil resulting from radiation damping or soil material

damping. One of the necessary conditions for radiation damping to occur is that the fundamental period of soil is not less than the effective fundamental period of the structure, in other words, the soil shear wave velocity is less than the shear wave velocity of the structure (Celebi 1996).

## **2.3 Seismic Isolation**

For most building structures, the natural periods are unfortunately within the range of typical earthquake ground motion-frequencies. The resonance of the structure with the ground motion may bring about tremendous damages. One potential way to reduce structural responses is to shift the natural period away from the dominant frequencies of earthquake ground motion. To this end, seismic isolation is the practice of lengthening the natural period of the structure by connecting the structure to its foundation via compliant rubber bearings or sliding bearings. Isolation bearings have the capacity for large deformations. Through recent decades of research, seismic isolation bearings have been developed into an increasingly popular method of seismic isolation (Kelly and Konstantinidis 2011). Seismic isolators are generally mounted at or near the base of the structure (Skinner et.al 1993). Ideally, when an earthquake attacks, the deformations occur mainly within the isolation system, and hence, the structure itself behaves more likely as a rigid body with limited deformations (Kelly 1997).

Various studies on instrumented base isolated structures have been conducted in recent decades. Dynamic behavior of base-isolated bridges and performance of isolation

bearings are evaluated through actual earthquake recordings during 1995 Kobe Earthquake. The analysis revealed that the base-isolation effects are prominent in instrumented bridges while friction element can degrade the base isolation effects considerably (ABE et al. 2000). The response records and the performance of the base-isolated USC hospital during 1994 Northridge Earthquake are examined (Celebi 1996, Nagarajaiah and Sun 2000). It turned out that the isolation system provided effective protection to the structure as was designed to. The key response quantities of base-isolated system are much less than corresponding fixed base superstructure (Asher, et al. 1995). In addition, after the E-Defense shaking table facility was completed in early 2005 in Japan, some full scale shake table tests on geostructures, wooden buildings, reinforced concrete buildings, steel building and bridges are being developed. Among these tests, the performance and effects of various dampers and isolation system are evaluated (Kasai et al. 2010).

A famous case study is the Olive View Hospital-UCLA Medical center located in California. Attacked by 1971's San Fernando Earthquake, the hospital's whole first story collapsed, from which the dangers of soft first story were recognized. The soft first story did make the building very flexible, however, it was too weak to bear large deformations. Having realized this drawback, the hospital was rebuilt with very strong steel shear walls. During 1994's Northridge Earthquake, the hospital indeed didn't collapse. Nonetheless, the violent shaking within the structure ripped out the sprinkler

system and induced the internal flooding. This happened because that the steel shear walls made the structure not flexible enough.

In conclusion, seismic isolation works via several mechanisms. First of all, the seismic isolation lengthens the natural period to be longer than the earthquake ground motion period. It should be noted that seismic isolation especially works well for sites far from a fault rupture. For the sites near a fault rupture, the ground can shake with a long period pulse which will presents potential problems for effective isolation. Second, seismic isolators can accommodate horizontal displacements at least 40cm to 60cm without failure. Third, seismic isolators can carry large gravity loads. For example, bearings are usually built-up from alternating layers of steel plates and rubber. When gravity loads are applied, the thin rubber layers (having a Poisson's ratio close to 0.5) are restrained from expanding radially by the steel plates to which they are laminated. The stiffness of the steel plates must be high enough to resist the radial expansions of the rubbers. Last but not the least, the large deformation capacity of the isolator allows for the accommodation of energy dissipation materials (lead core or mild steel), mechanism (friction), or devices (dampers). Lead core dampers, steel dampers, viscous dampers, friction dampers are all typically used dampers. The success of seismic isolation for a particular structure depends on the appropriate selection of the isolator components. An incorrectly chosen damper may negate the advantages of seismic isolation. For instance, a damper which brings too much damping induces too strong coupling between the

structure and the ground motion, which on the contrary makes the isolation less effective as well as creates potential problems for short-period shaking. Especially when considering the steady-state response, transmissibility at high frequencies can increase with higher damping levels in the isolation system. However, transient response peaks act as a more significant criterion in earthquake protection. This thesis addresses the question of the sensitivity of peak structural earthquake responses to the level of friction damping in the isolation system.

In this study, the sensitivity of the peak responses of seismic isolation systems to the soil shear wave velocity and friction damping in the isolation system will be investigated through numerical simulation and will be discussed.

## 3. Linear Soil Modeling and Interactions

### 3.1 Notation

In the linear soil modeling described in this section the soil is assumed to behave as a homogeneous and isotropic elastic half-space with simple viscoelastic damping. Soil deformations due to motion of a rigid circular pad of radius  $r_0$ , (the foundation) on the surface are assumed to be confined to a frustum, with an apex at a height of  $z_0$  above the surface (Wolf 1994). The dimensions of this “equivalent cone” (radius  $r_0$  at the surface, and apex at height  $z_0$ ) depend on the coordinate of motion of the pad (e.g., horizontal, vertical, rocking, twisting) and the dimensions of the actual foundation (which is typically rectangular), and the soil Poisson ratio. Given the dimensions of the cone for a particular coordinate of motion, and material characteristics (soil shear wave velocity, density, and Poisson ratio), equations approximating the stiffness and damping resisting motion in that coordinate can be evaluated. This procedure is detailed in the following.

The foundation for this study is rectangular, with dimensions of  $2a \times 2b \times d$  and with a total mass of  $M_F$ . The soil-foundation model in this study represents the behavior of a foundation in two coordinates: horizontal and rocking. This two-coordinate model is depicted in Figure 1, which shows how the soil foundation system can be modeled as a system of linear springs, dashpots and masses. The free-field ground translation is represented by  $w(t)$ ;  $\ddot{w}$  represents the translational disturbance accelerations induced from the free-field ground motion. The foundation can translate horizontally, denoted

by  $u_0$ . The soil is modeled with a horizontal stiffness of  $K$  in x-direction and with a parallel damping  $C$ . These two parameters are calculated using the following cone model concepts and the corresponding formulas. The rotational degree of freedom of the foundation about the axis along  $2b$  is  $\Phi$  at which the foundation node is connected by a rotational spring with the stiffness coefficient of  $K_\Phi$  and is paralleled by a rotational dashpot with the damping coefficient of  $C_\Phi$ . An additional rotational degree of freedom  $\Phi_1$  is introduced at which the node located between a rotational spring with the stiffness coefficient of  $-K_\Phi/3$  and a rotational dashpot with the damping coefficient of  $-C_\Phi$ . Negative values of these coefficients were found to match the solutions of a viscoelastic half-space model (Wolf 1994). The mass moment of inertia of the foundation is  $J_F$ . The base shear force  $V_b$  and base moment  $M_b$  resulting from the superstructure are applied to the top of the foundation. The superstructure is connected to the foundation via a base isolation system. The height of the base isolator above the foundation is  $h_1$ . The stiffness coefficient of the base isolator is  $k_1$  which is set to be 1/20 of the other floors. The nonlinear effects of base isolator is modeled through a hysteretic frictional force  $F_y$  between the foundation and the first floor above the base isolator. The heights between each floor above the base isolator are the same. The mass and the stiffness coefficient for each floor above the base isolator are the same.

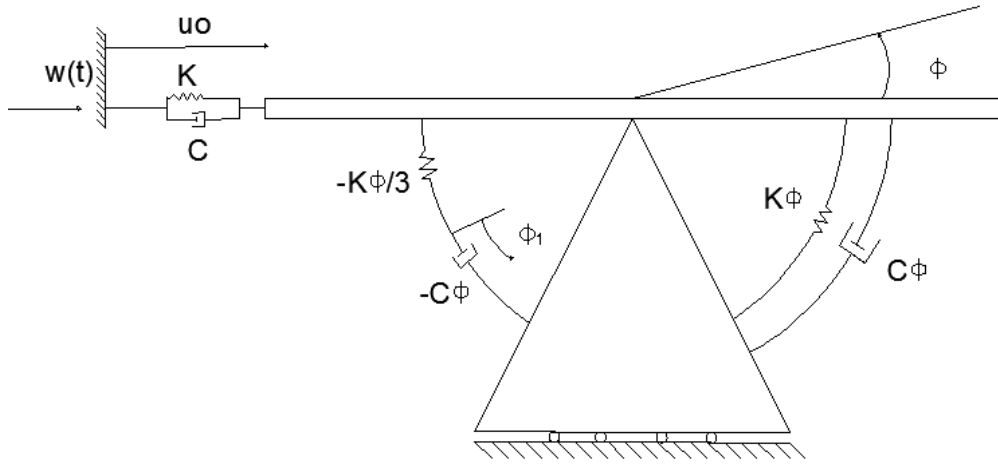
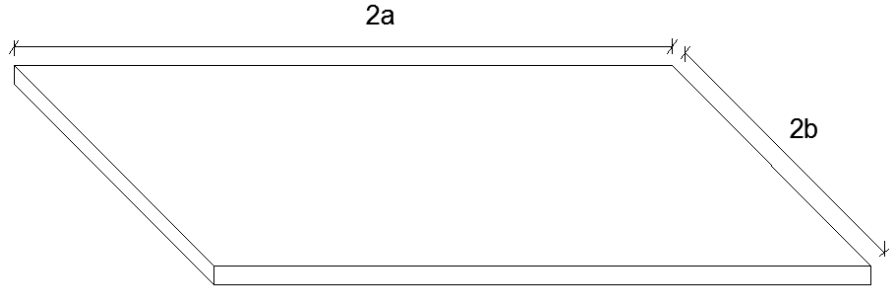


Figure 1: Physical model of the foundation system.

### 3.2 Construction of Cone Model

In this study, the soil is idealized as a homogeneous linearly elastic, semi-infinite medium with mass density of  $\rho$  and is idealized as a semi-infinite elastic cone with an apex height above grade of  $z_0$  for each degree of freedom. The equivalent disk radius  $r_0$  for horizontal stiffness is not the same as the radius for rocking stiffness.  $A_0$  is the circular area of the intersection of the horizontal ground surface and the cone and  $I_0$  is area moment of inertia for rocking cone. For a cone representing motion in the horizontal direction, the wave propagation velocity is specified to be the shear wave velocity, as  $c = c_s$ , which implies that the horizontal cone deforms in shear. While for the rocking cone, the wave propagation velocity is chosen as the pressure wave velocity,  $c = c_p$ , which implies that the rocking cone deforms by compression and extension of the soil. Wolf (1994) provides equations for the static soil-foundation stiffness  $K$ ,  $K_\phi$  and damping coefficient  $C$ ,  $C_\phi$ .



**Figure 2: Dimension of foundation.**

Horizontal motion:

$$r_0 = \frac{b}{8} \left[ 6.8 \left( \frac{a}{b} \right)^{0.65} + 0.8 \frac{a}{b} + 1.6 \right] \quad (3.1a)$$

$$A_0 = \pi r_0^2 \quad (3.1b)$$

$$z_0 = \frac{\pi}{8} r_0 (2 - \nu) \quad (3.1c)$$

$$c = c_s \quad (3.1d)$$

$$K = \rho c^2 A_0 / z_0 \quad (3.1e)$$

$$C = \rho c A_0 \quad (3.1f)$$

Rocking motion:

$$r_0^3 = \frac{3b^3}{8} \left[ 3.73 \left( \frac{a}{b} \right)^{2.4} + 0.27 \right] \quad (3.2a)$$

$$I_0 = \frac{1}{4} \pi r_0^4 \quad (3.2b)$$

$$z_0 = \frac{9\pi}{32} r_0 (1 - \nu) \left( \frac{c}{c_s} \right)^2 \quad (3.2c)$$

$$c = c_p = 2c_s \quad (3.2d)$$

$$K_\phi = 3\rho c^2 I_0 / z_0 \quad (3.2e)$$

$$C_\phi = \rho c I_0 \quad (3.2f)$$

Wolf (1994) determined these equations by matching the approximate cone model to an analytic solution of a rigid disk resting on the surface of a half space, in other words, by equating the static-stiffness coefficient of the cone model to the corresponding value of the half space.

### 3.3 Equations of Motion

Using Wolf's model for the soil-foundation system, the equations of motion of the soil-foundation and the structure are derived as follows.

#### 3.3.1 Soil-Foundation

For the soil-foundation coordinates  $\mathbf{X}_s = [u_0 \ u_0 \ \Phi \ \dot{\Phi} \ \Phi_1]^T$ , the equations of motion are

$$\sum F_x = 0, M_F \ddot{u}_0 + C \dot{u}_0 + K u_0 = -M_F \ddot{w} + V_b \quad (3.3)$$

$$\sum M_\Phi = 0, J_F \ddot{\Phi} + C_\Phi \dot{\Phi} + K_\Phi \Phi - \frac{K_\Phi}{3} (\Phi - \Phi_1) = M_b \quad (3.4)$$

$$-\frac{K_\Phi}{3} (\Phi_1 - \Phi) - C_\Phi \dot{\Phi}_1 = 0 \quad (3.5)$$

The soil-foundation equations of motion may be represented in matrix form as follows:

$$\dot{\mathbf{X}}_s = \mathbf{A}_s \mathbf{X}_s + \mathbf{B}_w \ddot{w} + \mathbf{B}_v V_b + \mathbf{B}_M M_b \quad (3.6)$$

where

$$\mathbf{A}_s = \begin{bmatrix} 0 & 1 & 0 & 0 & 0 \\ -K/M_F & -C/M_F & 0 & 0 & 0 \\ 0 & 0 & 0 & 1 & 0 \\ 0 & 0 & -2K_\Phi/(3J_F) & -C_\Phi/J_F & K_\Phi/(3J_F) \\ 0 & 0 & K_\Phi/(3C_\Phi) & 0 & -K_\Phi/(3C_\Phi) \end{bmatrix}$$

$$\mathbf{B}_w = [0 \ -1 \ 0 \ 0 \ 0]^T, \mathbf{B}_v = [0 \ \frac{1}{M_F} \ 0 \ 0 \ 0]^T, \mathbf{B}_M = [0 \ 0 \ 0 \ \frac{1}{J_F} \ 0]^T$$

$V_b$  is termed as the base shear and  $M_b$  is the base bending moment.

### 3.3.2 Superstructure

The model for the superstructure connected to the foundation through base isolator is determined. Figure 3 depicts the structural system. The height of the base isolator is  $h_1$ . The  $i$ th story has height  $h_i$  from the foundation and each story has a same mass  $m$ .

For the structural system coordinates,  $\mathbf{X}_b = [u_1 \ u_2 \ u_3 \ u_4 \ u'_1 \ u'_2 \ u'_3 \ u'_4]^T$ ,  $z$  is the shape of the scaled friction function,  $z = F_f/f_y$ , and  $F_f$  is the hysteretic restoring friction force between the foundation and the first floor.

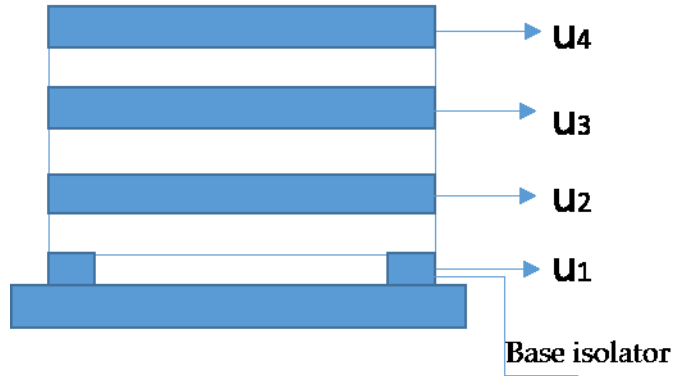


**Figure 3: Visual representation of 1-D model.**

The hysteretic friction force evolves according to the first order nonlinear differential equation.

$$\dot{z} = (1 - |z|^n(\alpha \text{sign}(uz) + \beta))\dot{u} \quad (3.7)$$

Where

$$z = F_f / f_y$$

$$\dot{u} = \dot{u}_1 / r_y$$

$$n = 2, \alpha = 0.9, \beta = 0.1$$

The mass matrix is diagonal,

$$\mathbf{M}_B = \text{diag}[m_1, m_2, m_3, m_4]$$

$$M_T = \sum_1^4 m_i$$

The stiffness matrix is tri-diagonal,

$$\mathbf{K}_B = \begin{bmatrix} K_1 + K_2 & -K_2 & 0 & 0 \\ -K_2 & K_2 + K_3 & -K_3 & 0 \\ 0 & -K_3 & K_3 + K_4 & -K_4 \\ 0 & 0 & -K_4 & K_4 \end{bmatrix}$$

Rayleigh Light damping is assumed for the superstructure giving modal damping ratios of 4%.

$$\mathbf{C}_B = \alpha' \mathbf{M}_B + \beta' \mathbf{K}_B$$

$$\alpha' = 0.2/s, \beta' = 0.001s$$

The structural system equations of motion may be represented in matrix form as follows:

$$\mathbf{X}_b \dot{\phantom{x}} = \mathbf{A}_b \mathbf{X}_b + \mathbf{B}_{FZ} z + \mathbf{B}_b \ddot{w} + \mathbf{B}_b \ddot{u}_0 + \mathbf{B}_\phi \ddot{\phi} \quad (3.8)$$

where

$$\mathbf{A}_b = \begin{bmatrix} \mathbf{0}_{4 \times 4} & \mathbf{I}_{4 \times 4} \\ -\mathbf{M}_B^{-1} \mathbf{K}_B & -\mathbf{M}_B^{-1} \mathbf{C}_B \end{bmatrix}$$

$$\mathbf{B}_F = [0 \ 0 \ 0 \ 0 \ -\frac{f_y}{m_1} \ 0 \ 0 \ 0]^T$$

$$\mathbf{B}_b = \begin{bmatrix} \mathbf{0}_{4 \times 1} \\ -\mathbf{1}_{4 \times 1} \end{bmatrix}$$

$$\mathbf{B}_\Phi = \begin{bmatrix} \mathbf{0}_{4 \times 1} \\ h_1 \\ h_2 \\ h_3 \\ h_4 \end{bmatrix}$$

### 3.4 State Space

In this section we combine the soil-foundation system model with the superstructure system model. The augmented model state space equations can be developed through coupling these two systems.

The base shear  $V_b$  and overturning moment  $M_b$ , are external forces affecting the soil-foundation system. The forces transmitted through the base isolator system but can be found from the total superstructure accelerations.

$$-V_b = \sum_1^4 m_i (\ddot{u}_0 + \ddot{w}) - \sum_1^4 m_i h_i \ddot{\Phi} + [m_1 \ m_2 \ m_3 \ m_4][\ddot{u}_1 \ \ddot{u}_2 \ \ddot{u}_3 \ \ddot{u}_4]^T \quad (3.9)$$

$$-M_b = \sum_1^4 m_i h_i (\ddot{u}_0 + \ddot{w}) - \sum_1^4 m_i h_i^2 \ddot{\Phi} + [m_1 h_1 \ m_2 h_2 \ m_3 h_3 \ m_4 h_4][\ddot{u}_1 \ \ddot{u}_2 \ \ddot{u}_3 \ \ddot{u}_4]^T \quad (3.10)$$

Let  $C_2, C_4$  be the second row and fourth row of the  $\mathbf{A}_s$  matrix. Then we have

$$\ddot{u}_0 + \ddot{w} = C_2 \mathbf{X}_s + V_b/M_F \quad (3.11)$$

$$\ddot{\Phi} = C_4 \mathbf{X}_s + M_b/J_F \quad (3.12)$$

Plug (3.11) and (3.12) back in (3.8), the structure system state-space may be represented as

$$\dot{\mathbf{X}}_b = \mathbf{A}_b \mathbf{X}_b + \mathbf{B}_{FZ} + \mathbf{B}_b (C_2 \mathbf{X}_s + V_b/M_F) + \mathbf{B}_\Phi (C_4 \mathbf{X}_s + M_b/J_F) \quad (3.13)$$

Substitute (3.11) and (3.12) back in (3.9) and (3.10), then solve these two equations and the following expressions can be obtained

$$V_b = V_1 \mathbf{X}_s + V_2 [\ddot{u}_1 \ddot{u}_2 \ddot{u}_3 \ddot{u}_4]^T \quad (3.14)$$

$$M_b = M_1 \mathbf{X}_s + M_2 [\ddot{u}_1 \ddot{u}_2 \ddot{u}_3 \ddot{u}_4]^T \quad (3.15)$$

Then plug (3.14) and (3.15) into (3.6) and (3.13),

$$\begin{aligned} \dot{\mathbf{X}}_s &= [\mathbf{A}_s + \mathbf{B}_v V_1 + \mathbf{B}_M M_1] \mathbf{X}_s + \mathbf{B}_w \ddot{w} + [\mathbf{B}_v V_2 + \mathbf{B}_M M_2] [\ddot{u}_1 \ddot{u}_2 \ddot{u}_3 \ddot{u}_4]^T \\ &= [\mathbf{A}_s + \mathbf{B}_v V_1 + \mathbf{B}_M M_1] \mathbf{X}_s + \mathbf{B}_w \ddot{w} + [\mathbf{0}_{5 \times 4} \quad \mathbf{B}_v V_2 + \mathbf{B}_M M_2] \dot{\mathbf{X}}_b \end{aligned} \quad (3.16)$$

$$\begin{aligned} \dot{\mathbf{X}}_b &= \mathbf{A}_b \mathbf{X}_b + \mathbf{B}_{FZ} + \mathbf{B}_b \left[ C_2 \mathbf{X}_s - \frac{[V_1 \mathbf{X}_s + V_2 [\ddot{u}_1 \ddot{u}_2 \ddot{u}_3 \ddot{u}_4]^T]}{M_F} \right] + \mathbf{B}_\Phi [C_4 \mathbf{X}_s \\ &\quad + \frac{[M_1 \mathbf{X}_s + M_2 [\ddot{u}_1 \ddot{u}_2 \ddot{u}_3 \ddot{u}_4]^T]}{J_F}] \\ &= \mathbf{A}_b \mathbf{X}_b + \mathbf{B}_{FZ} + \left[ \mathbf{B}_b C_2 - \frac{\mathbf{B}_b V_1}{M_F} + \mathbf{B}_\Phi C_4 + \frac{\mathbf{B}_\Phi M_1}{J_F} \right] \mathbf{X}_s + \left[ -\frac{\mathbf{B}_b V_2}{M_F} + \frac{\mathbf{B}_\Phi M_2}{J_F} \right] [\ddot{u}_1 \ddot{u}_2 \ddot{u}_3 \ddot{u}_4]^T \\ &= \mathbf{A}_b \mathbf{X}_b + \mathbf{B}_{FZ} + \left[ \mathbf{B}_b C_2 - \frac{\mathbf{B}_b V_1}{M_F} + \mathbf{B}_\Phi C_4 + \frac{\mathbf{B}_\Phi M_1}{J_F} \right] \mathbf{X}_s + \left[ \mathbf{0}_{8 \times 4} \quad -\frac{\mathbf{B}_b V_2}{M_F} + \frac{\mathbf{B}_\Phi M_2}{J_F} \right] \dot{\mathbf{X}}_b \end{aligned} \quad (3.17)$$

$$\text{Define } \mathbf{Q}_1 = \left[ I_{8 \times 8} \quad - \left[ \mathbf{0}_{8 \times 4} \quad -\frac{\mathbf{B}_b V_2}{M_F} + \frac{\mathbf{B}_\Phi M_2}{J_F} \right] \right]^{-1}$$

$$\dot{\mathbf{X}}_b = \mathbf{Q}_1 \mathbf{A}_b \mathbf{X}_b + \mathbf{Q}_1 \mathbf{B}_{FZ} + \mathbf{Q}_1 \left[ \mathbf{B}_b C_2 - \frac{\mathbf{B}_b V_1}{M_F} + \mathbf{B}_\Phi C_4 + \frac{\mathbf{B}_\Phi M_1}{J_F} \right] \mathbf{X}_s \quad (3.18)$$

$$\text{Define } \mathbf{Q}_2 = \mathbf{Q}_1 \left[ \mathbf{B}_b C_2 - \frac{\mathbf{B}_b V_1}{M_F} + \mathbf{B}_\Phi C_4 + \frac{\mathbf{B}_\Phi M_1}{J_F} \right]$$

$$\dot{X}_b = \mathbf{Q}_1 \mathbf{A}_b X_b + \mathbf{Q}_1 \mathbf{B}_{FZ} + \mathbf{Q}_2 X_s \quad (3.19)$$

$$\begin{aligned} \dot{X}_s &= [\mathbf{A}_s + \mathbf{B}_v V_1 + \mathbf{B}_M M_1] X_s + \mathbf{B}_w \ddot{w} + [\mathbf{0}_{5 \times 4} \quad \mathbf{B}_v V_2 + \mathbf{B}_M M_2] [\mathbf{Q}_1 \mathbf{A}_b X_b + \mathbf{Q}_1 \mathbf{B}_{FZ} + \mathbf{Q}_2 X_s] \\ &= [\mathbf{A}_s + \mathbf{B}_v V_1 + \mathbf{B}_M M_1 + [\mathbf{0}_{5 \times 4} \quad \mathbf{B}_v V_2 + \mathbf{B}_M M_2] \mathbf{Q}_2] X_s + \mathbf{B}_w \ddot{w} + [\mathbf{0}_{5 \times 4} \quad \mathbf{B}_v V_2 + \\ &\quad \mathbf{B}_M M_2] \mathbf{Q}_1 \mathbf{A}_b X_b [\mathbf{0}_{5 \times 4} \quad \mathbf{B}_v V_2 + \mathbf{B}_M M_2] \mathbf{Q}_1 \mathbf{B}_{FZ} \end{aligned} \quad (3.20)$$

Define  $\mathbf{Q}_{s1} = [\mathbf{A}_s + \mathbf{B}_v V_1 + \mathbf{B}_M M_1 + [\mathbf{0}_{5 \times 4} \quad \mathbf{B}_v V_2 + \mathbf{B}_M M_2] \mathbf{Q}_2]$   $\mathbf{Q}_{s2} =$   
 $[\mathbf{0}_{5 \times 4} \quad \mathbf{B}_v V_2 + \mathbf{B}_M M_2] \mathbf{Q}_1 \mathbf{A}_b$   
 $\mathbf{Q}_{s3} = [\mathbf{0}_{5 \times 4} \quad \mathbf{B}_v V_2 + \mathbf{B}_M M_2] \mathbf{Q}_1 \mathbf{B}_F$

$$\dot{X}_s = \mathbf{Q}_{s1} X_s + \mathbf{B}_w \ddot{w} + \mathbf{Q}_{s2} X_b + \mathbf{Q}_{s3} Z \quad (3.21)$$

Augmenting the two state-spaces, the full soil foundation structure space model is

$$\begin{aligned} \dot{X} &= \begin{bmatrix} \dot{X}_s \\ \dot{X}_b \end{bmatrix} = \begin{bmatrix} \mathbf{Q}_{s1} & \mathbf{Q}_{s2} \\ \mathbf{Q}_2 & \mathbf{Q}_1 \mathbf{A}_b \end{bmatrix} \begin{bmatrix} X_s \\ X_b \end{bmatrix} + \begin{bmatrix} \mathbf{B}_w & \mathbf{Q}_{s3} \\ \mathbf{0}_{8 \times 1} & \mathbf{Q}_1 \mathbf{B}_F \end{bmatrix} \begin{bmatrix} \ddot{w} \\ Z \end{bmatrix} \\ &= \mathbf{A} X + \mathbf{B} u \end{aligned} \quad (3.22)$$

### 3.5 Numerical Procedure with MATLAB

In this section, the linear soil model coupled with a four story structure is modeled in MATLAB. The first story represents the base isolation system. Three examples are implemented primarily to investigate the soil-foundation-structure interaction. The principal structure is designed to be the same for these three examples. In example 1 and 2, the isolation system characteristics are the same, however, the soil

properties are different. In example 2 and 3, the soil properties are designed to be the same, the isolation systems feature differently.

### 3.5.1 Example 1: 100 m/s shear wave velocity, low frictional force

In this numerical example, a synthetic ground motion is generated that is representative of a far-field earthquake (Scruggs and Gavin 2010). Table 1 describes all the parameters used in this numerical model, including soil properties, foundation properties and the superstructure properties. It's worth noting that in this numerical example, the soil shear wave velocity being used is around 100 m/s which is very low. According to soil type classifications defined by NEHRP, the soil used in this model belongs to "type E" (soft soil).

In addition, a hysteretic force used to model the effects of friction on the base isolated system is very low and is around 1 percent of the total superstructure weight.

**Table 1: Parameters used to design the whole system.**

<b>Soil properties</b>		
Density ( $kg/m^3$ )	$\rho$	1800
Poisson's ratio	$\nu$	1/3
Shear wave velocity ( $m/s$ )	$C_s$	100
<b>Foundation properties</b>		
Length ( $m$ , along x-axis)	$2a$	70
Width ( $m$ , along y-axis)	$2b$	30
Thickness ( $m$ )	$d$	2
Mass ( $kg$ )	$M_F$	$1.008 \times 10^7$
Moment of inertia( $kg \cdot m^2$ )	$J_F$	$4.872 \times 10^9$
<b>Structure properties</b>		
<b>Base isolator</b>		
Mass ( $kg$ )	$m_1$	$2.016 \times 10^6$
Stiffness ( $N/m$ )	$k_1$	$0.05 \times 10^9$

Height ( $m$ )	$h_1$	2
Hysteretic friction force scaling factors		
% of the total mass ( $kN$ )	$f_v/M_T/g$	0.01
( $m$ )	$r_Y$	0.005
Second story		
Mass ( $kg$ )	$m_2$	$2.016 \times 10^6$
Stiffness ( $N/m$ )	$k_2$	$1.00 \times 10^9$
Height ( $m$ )	$h_2$	5
Third story		
Mass ( $kg$ )	$m_3$	$2.016 \times 10^6$
Stiffness ( $N/m$ )	$k_3$	$1.00 \times 10^9$
Height ( $m$ )	$h_3$	8
Fourth story		
Mass ( $kg$ )	$m_4$	$2.016 \times 10^6$
Stiffness ( $N/m$ )	$k_4$	$1.00 \times 10^9$
Height ( $m$ )	$h_4$	11

An eigenvalue analysis is conducted for the dynamic matrix of both systems. The real parts of the eigenvalues are all negative for each system guarantees that each part of the system as well as the whole system are stable and behave like a damped oscillator. Therefore, the system will get back to static equilibrium, no matter how it is forced.

The results for natural frequencies and damping factors for the soil-foundation system, superstructure system and the whole system are reported in table 2, 3 and 4 respectively. Regarding the natural frequency results in table 3 and 4, the corresponding fundamental natural frequency values are reduced obviously for the superstructure system when it is assembled into the whole system. This implies that the SSI effect slightly lengthens the period of the isolated superstructure in this model.

The following figures are described in the discussion section below.

**Table 2: Natural frequency and damping factor for soil-foundation system (Example 1).**

Natural Frequency (cyc/sec)	Damping	Damped Frequency (cyc/sec)	Eigenvalue	
			real	imag
0.73009	0.86601	0.36507	-3.97262	2.29378
0.73009	0.86601	0.36507	-3.97262	2.29378
0.98157	1.00000	0.00000	-6.16741	0.00000
6.32952	1.00000	0.00000	-39.76952	0.00000
12.32726	1.00000	0.00000	-77.45443	0.00000

**Table 3: Natural frequency and damping factor for superstructure system (Example 1).**

Natural Frequency (cyc/sec)	Damping	Damped Frequency (cyc/sec)	Eigenvalue	
			real	imag
0.38776	0.04226	0.38742	-0.10297	2.43420
0.38776	0.04226	0.38742	-0.10297	-2.43420
2.76244	0.01444	2.76216	-0.25063	17.35514
2.76244	0.01444	2.76216	-0.25063	-17.35514
5.02885	0.01896	5.02794	-0.59919	31.59149
5.02885	0.01896	5.02794	-0.59919	-31.59149
6.55326	0.02302	6.55153	-0.94771	41.16447
6.55326	0.02302	6.55153	-0.94771	-41.16447

**Table 4: Natural frequency and damping factor for the whole system (Example 1).**

Natural Frequency (cyc/sec)	Damping	Damped Frequency (cyc/sec)	Eigenvalue	
			real	imag
0.23972	0.02694	0.23964	-0.04058	1.50567
0.23972	0.02694	0.23964	-0.04058	-1.50567
0.72947	0.86587	0.36493	-3.96859	2.29293
0.72947	0.86587	0.36493	-3.96859	-2.29293
0.98810	1.00000	0.00000	-6.20844	0.00000
2.76255	0.01231	2.76234	-0.21374	17.35630
2.76255	0.01231	2.76234	-0.21374	-17.35630

5.02879	0.01897	5.02789	-0.59929	31.59115
5.02879	0.01897	5.02789	-0.59929	-31.59115
6.33251	1.00000	0.00000	-39.78833	0.00000
6.55320	0.02299	6.55147	-0.94667	41.16411
6.55320	0.02299	6.55147	-0.94667	-41.16411
12.33807	1.00000	0.00000	-77.52237	0.00000

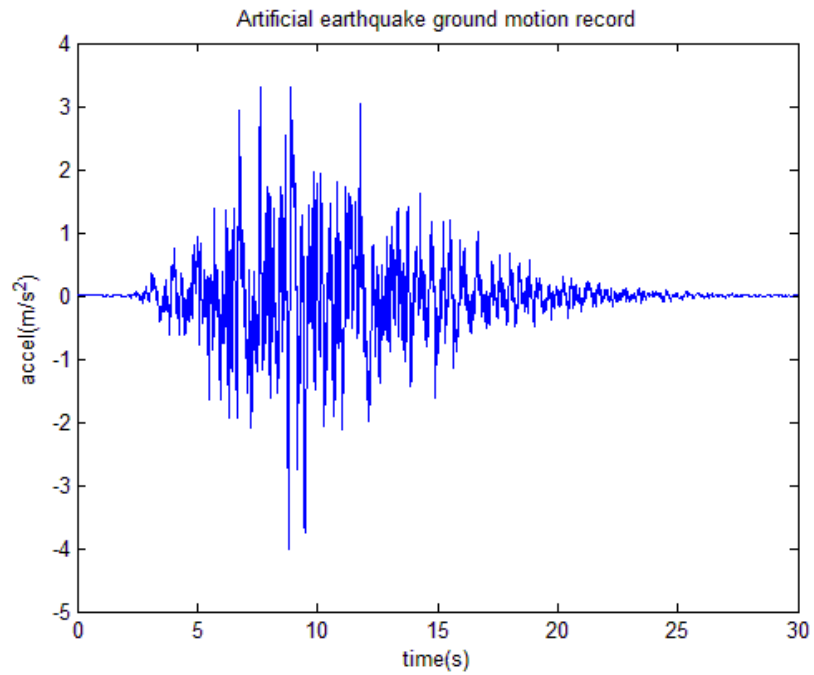


**Figure 4: Artificial far field ground motion record (Example 1).**

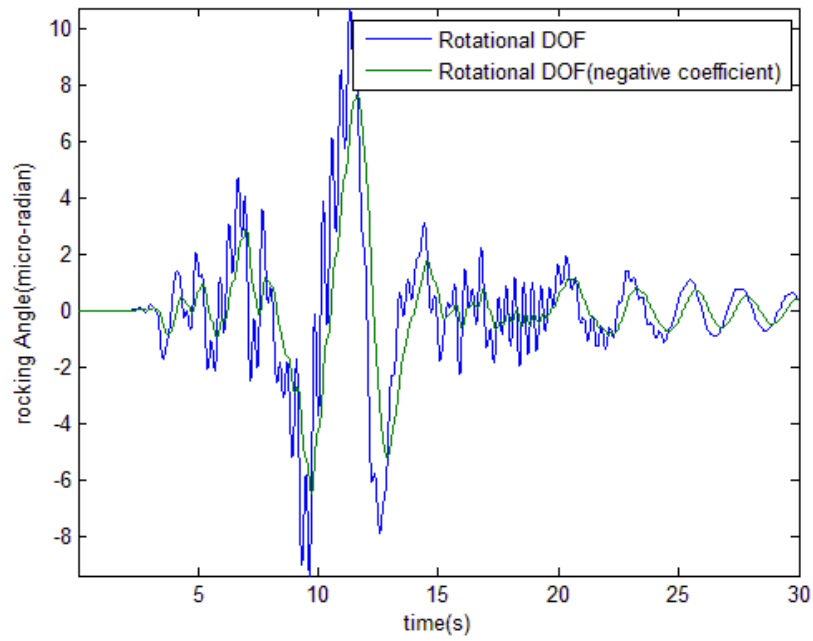


Figure 5: Displacement and velocity response for soil and each floor (Example 1).

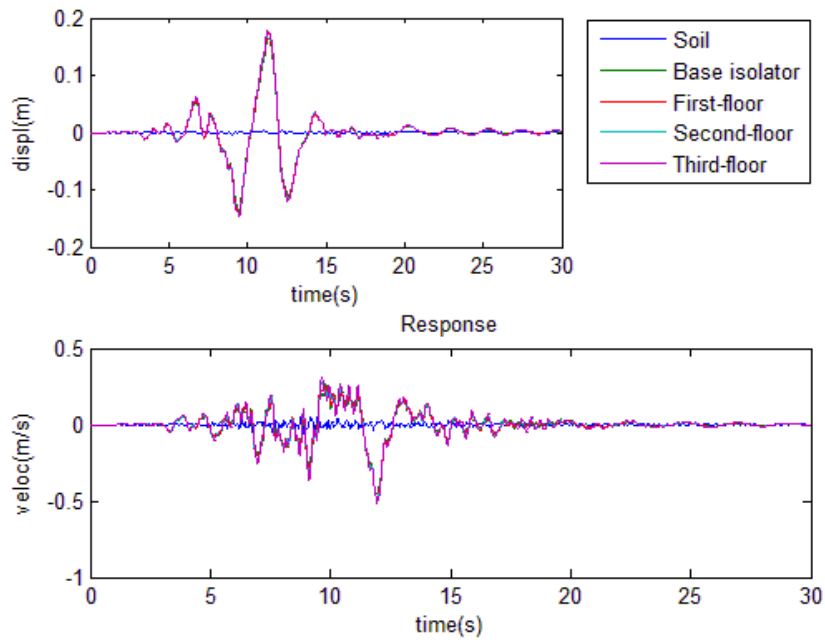


Figure 6: Two rocking degrees of freedom response (Example 1).

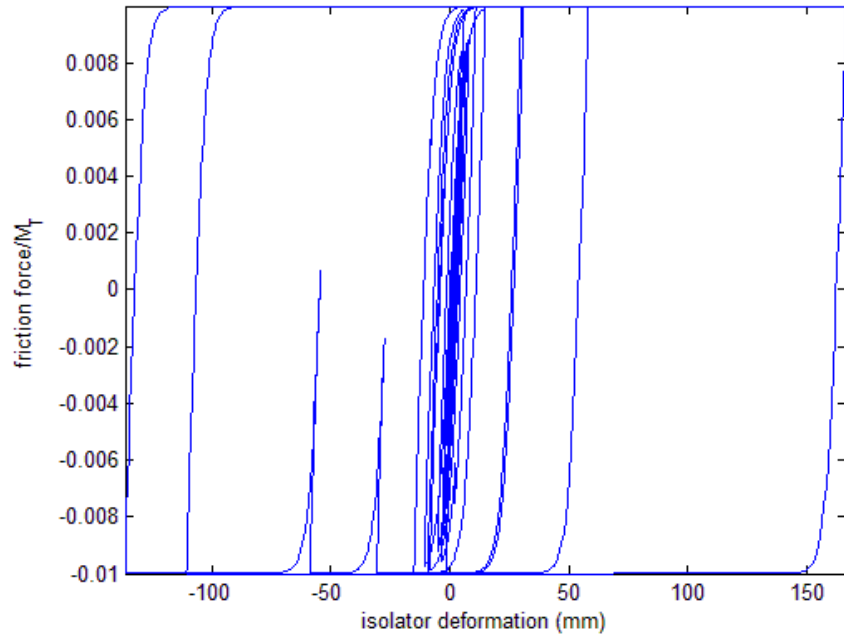


Figure 7: Hysteresis loop (Example 1).

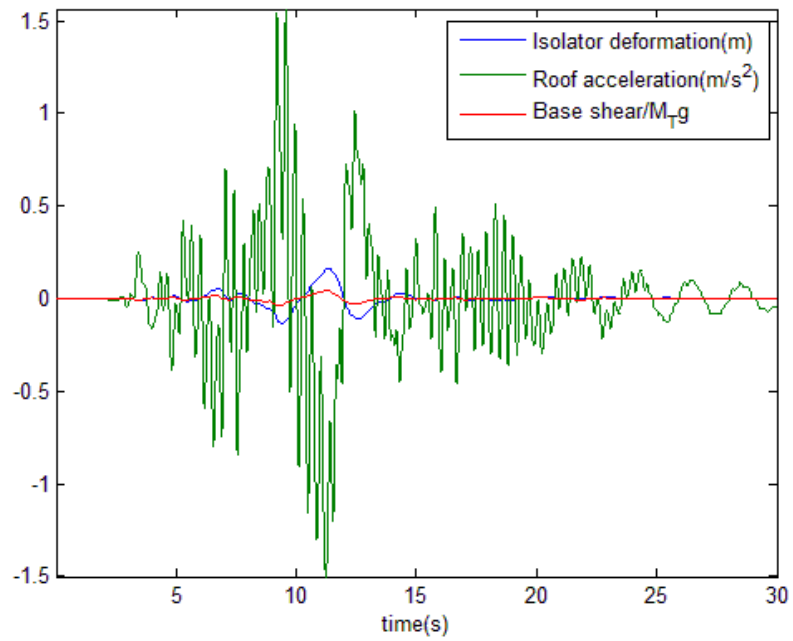


Figure 8: Base isolator deformation, roof acceleration, and base shear ratio

**(Example 1).**

### **3.5.2 Example 2: 200 m/s shear wave velocity, low frictional force**

In this example we increase the soil shear wave velocity from 100 m/s to 200 m/s, and keep the other parameters and properties exactly the same as in example 1.

According to soil type classifications defined by NEHRP, the soil used in this model belongs to “type D” which is termed as stiff soil.

Similarly, an eigenvalue analysis is conducted for each system stiffness matrix. Again, the real parts of the eigenvalues are all negative for each system, guaranteeing that each part of the system as well as the whole system are stable and behave like a damped oscillator. Therefore, the system will reach static equilibrium no matter how it is forced.

The results for natural frequencies and damping factors for the soil-foundation system, superstructure system and the whole system are reported in table 5, 6 and 7 respectively. Comparing natural frequency results in table 6 and 7, the corresponding fundamental natural frequency values are reduced significantly for the superstructure system when assembled into the whole system. This implies that SSI effect lengthens the natural period of the isolated superstructure in this model.

In addition, comparing table 3 and table 6, the results are exactly the same. As expected, the shear wave velocity doesn't affect the natural frequencies of the

superstructure system, it only affects natural frequencies and the stiffness of the soil-foundation system.

Comparing the differences between table 2 and table 5, it can be inferred that higher shear wave velocity results in larger natural frequencies of the soil-foundation system, as would be expected.

**Table 5: Natural frequency and damping factor for soil-foundation system (Example 2).**

Natural Frequency (cyc/sec)	Damping	Damped Frequency (cyc/sec)	Eigenvalue	
			real	imag
1.46018	0.86601	0.73013	-7.94525	4.58756
1.46018	0.86601	0.73013	-7.94525	-4.58756
1.96315	1.00000	0.00000	-12.3348	0.00000
12.65903	1.00000	0.00000	-79.539	0.00000
24.65451	1.00000	0.00000	-154.909	0.00000

**Table 6: Natural frequency and damping factor for superstructure system (Example 2).**

Natural Frequency (cyc/sec)	Damping	Damped Frequency (cyc/sec)	Eigenvalue	
			real	imag
0.38776	0.04226	0.38742	-0.10297	2.4342
0.38776	0.04226	0.38742	-0.10297	-2.4342
2.76244	0.01444	2.76216	-0.25063	17.35514
2.76244	0.01444	2.76216	-0.25063	-17.3551
5.02885	0.01896	5.02794	-0.59919	31.59149
5.02885	0.01896	5.02794	-0.59919	-31.5915
6.55326	0.02302	6.55153	-0.94771	41.16447
6.55326	0.02302	6.55153	-0.94771	-41.1645

**Table 7: Natural frequency and damping factor for the whole system (Example 2).**

Natural Frequency (cyc/sec)	Damping	Damped Frequency (cyc/sec)	Eigenvalue	
			real	imag
0.24032	0.02628	0.24024	-0.03968	1.50948
0.24032	0.02628	0.24024	-0.03968	-1.50948
1.45923	0.86591	0.72990	-7.93922	4.58610
1.45923	0.86591	0.72990	-7.93922	-4.58610
1.96566	1.00000	0.00000	-12.35059	0.00000
2.76325	0.01358	2.76300	-0.23573	17.36041
2.76325	0.01358	2.76300	-0.23573	-17.36041
5.02878	0.01897	5.02788	-0.59924	31.59110
5.02878	0.01897	5.02788	-0.59924	-31.59110
6.55326	0.02300	6.55153	-0.94713	41.16446
6.55326	0.02300	6.55153	-0.94713	-41.16446
12.66648	1.00000	0.00000	-79.58585	0.00000
24.65868	1.00000	0.00000	-154.93504	0.00000

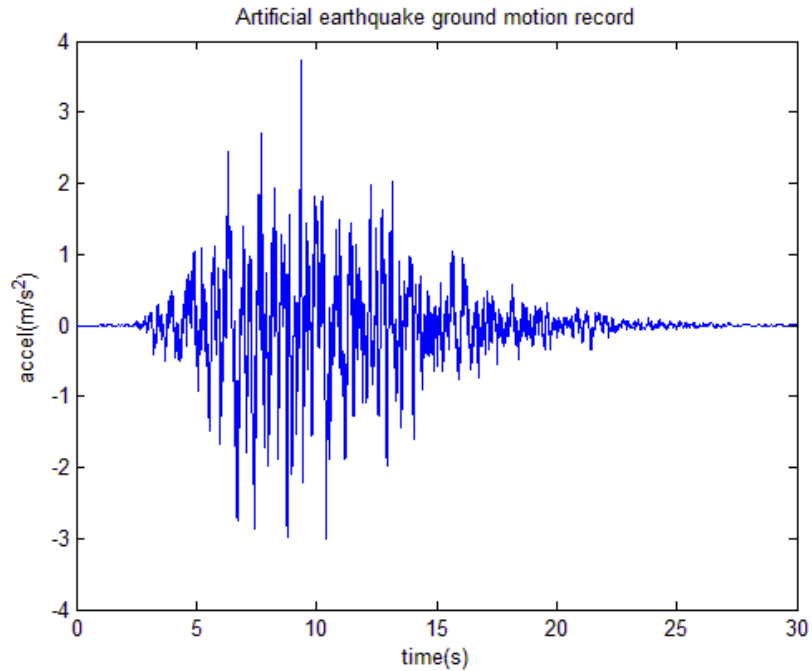


**Figure 9: Artificial far field ground motion record (Example 2).**

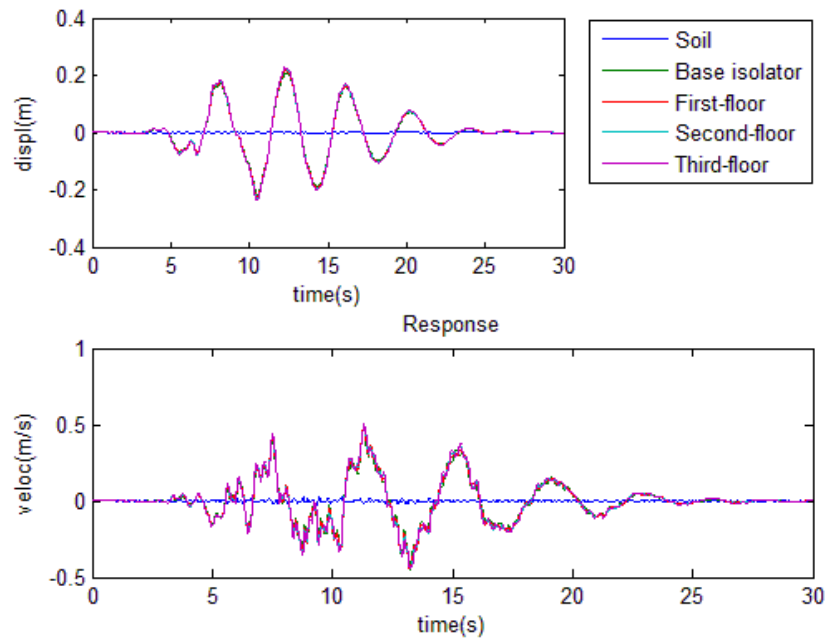


Figure 10: Displacement and velocity response for soil and each floor (Example 2).

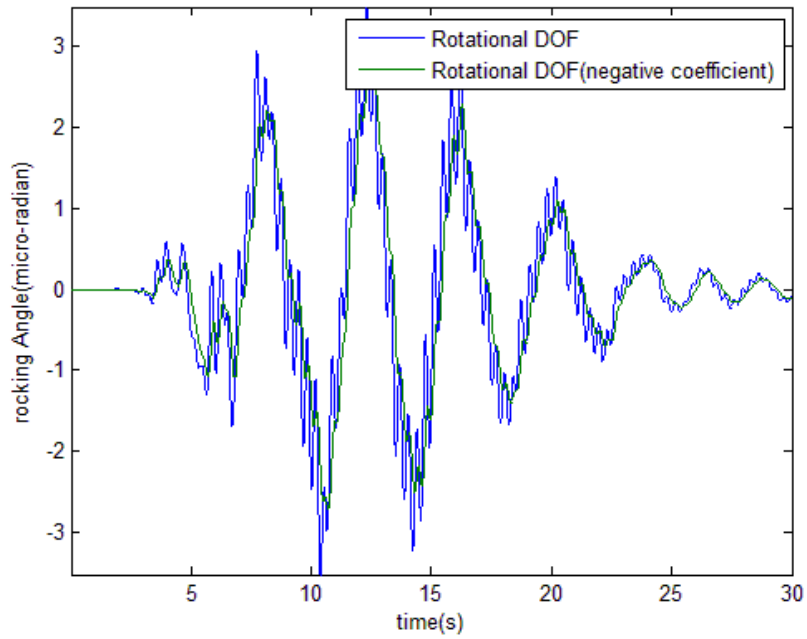
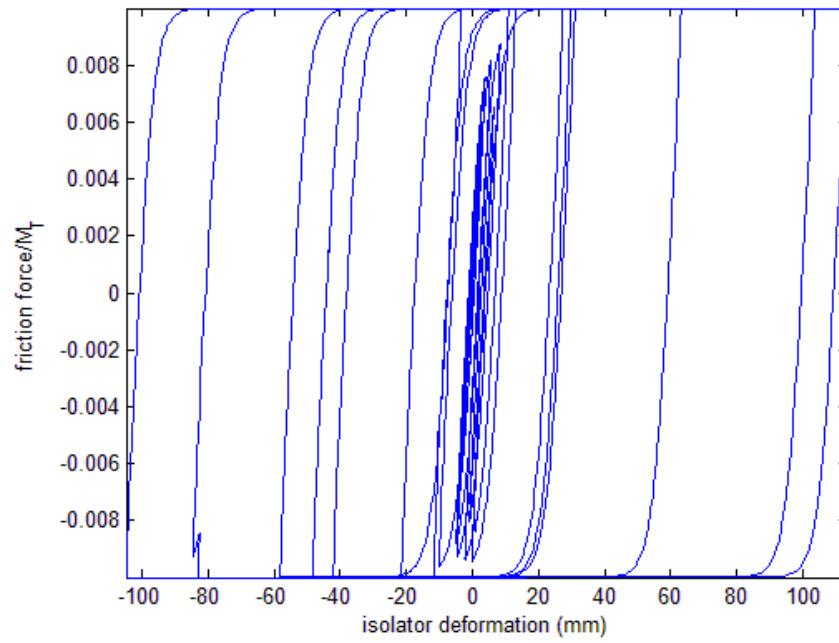
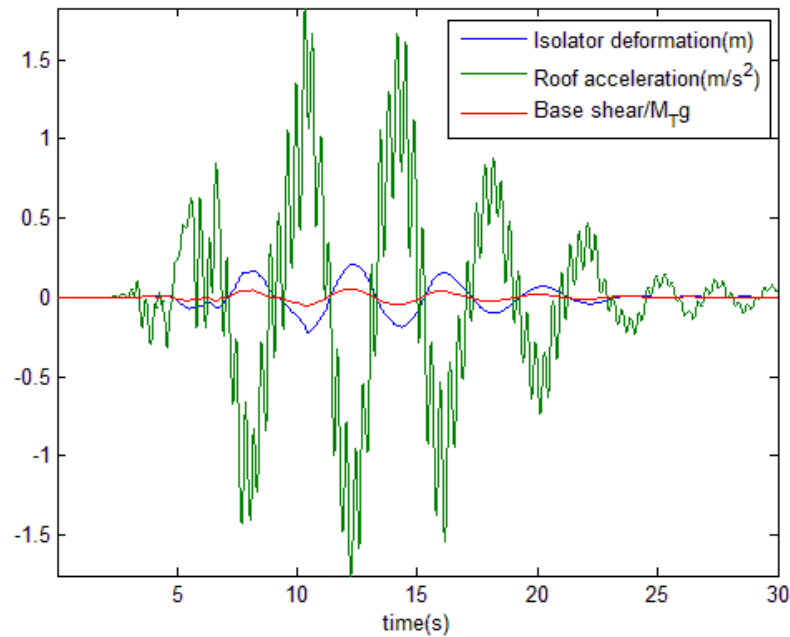


Figure 11: Two rocking degrees of freedom response (Example 2).



**Figure 12: Hysteresis loop (Example 2).**



**Figure 13: Base isolator deformation, roof acceleration, and base shear ratio. (Example 2)**

### **3.5.3 Example 3: 200 m/s shear wave velocity, high frictional force**

The analysis is repeated after increasing the nonlinear hysteretic frictional force between the foundation and first floor up to 20 percent of the total superstructure weight, and keeping other parameters and properties exactly the same as in example 2.

The results for natural frequencies and damping factors for the soil-foundation system, superstructure system and the whole system are reported in Tables 8, 9 and 10 respectively. The results obtained are exactly the same as those in example 2. This shows that the nonlinear frictional force doesn't affect the assembly of the system matrix for each part of the structure system.

**Table 8: Natural frequency and damping factor for soil-foundation system (Example 3).**

Natural Frequency (cyc/sec)	Damping	Damped Frequency (cyc/sec)	Eigenvalue	
			real	imag
1.46018	0.86601	0.73013	-7.94525	4.58756
1.46018	0.86601	0.73013	-7.94525	-4.58756
1.96315	1.00000	0.00000	-12.3348	0.00000
12.65903	1.00000	0.00000	-79.539	0.00000
24.65451	1.00000	0.00000	-154.909	0.00000

**Table 9: Natural frequency and damping factor for superstructure system (Example 3).**

Natural Frequency (cyc/sec)	Damping	Damped Frequency (cyc/sec)	Eigenvalue	
			real	imag
0.38776	0.04226	0.38742	-0.10297	2.4342
0.38776	0.04226	0.38742	-0.10297	-2.4342
2.76244	0.01444	2.76216	-0.25063	17.35514
2.76244	0.01444	2.76216	-0.25063	-17.3551
5.02885	0.01896	5.02794	-0.59919	31.59149
5.02885	0.01896	5.02794	-0.59919	-31.5915
6.55326	0.02302	6.55153	-0.94771	41.16447
6.55326	0.02302	6.55153	-0.94771	-41.1645

**Table 10: Natural frequency and damping factor for the whole system (Example 3).**

Natural Frequency (cyc/sec)	Damping	Damped Frequency (cyc/sec)	Eigenvalue	
			real	imag
0.24032	0.02628	0.24024	-0.03968	1.50948
0.24032	0.02628	0.24024	-0.03968	-1.50948
1.45923	0.86591	0.72990	-7.93922	4.58610
1.45923	0.86591	0.72990	-7.93922	-4.58610
1.96566	1.00000	0.00000	-12.35059	0.00000
2.76325	0.01358	2.76300	-0.23573	17.36041
2.76325	0.01358	2.76300	-0.23573	-17.36041
5.02878	0.01897	5.02788	-0.59924	31.59110

5.02878	0.01897	5.02788	-0.59924	-31.59110
6.55326	0.02300	6.55153	-0.94713	41.16446
6.55326	0.02300	6.55153	-0.94713	-41.16446
12.66648	1.00000	0.00000	-79.58585	0.00000
24.65868	1.00000	0.00000	-154.93504	0.00000

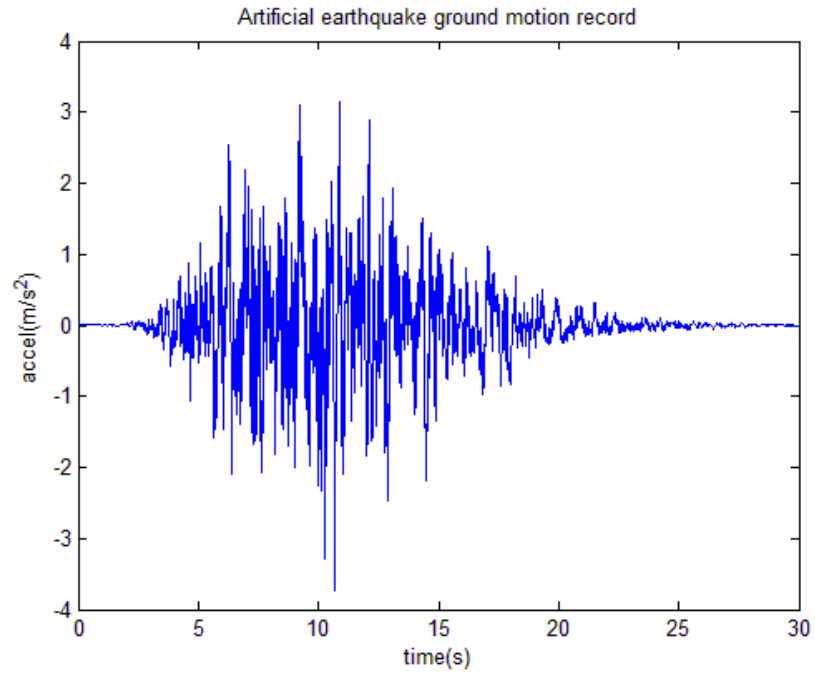


**Figure 14: Artificial far field ground motion record (Example 3).**

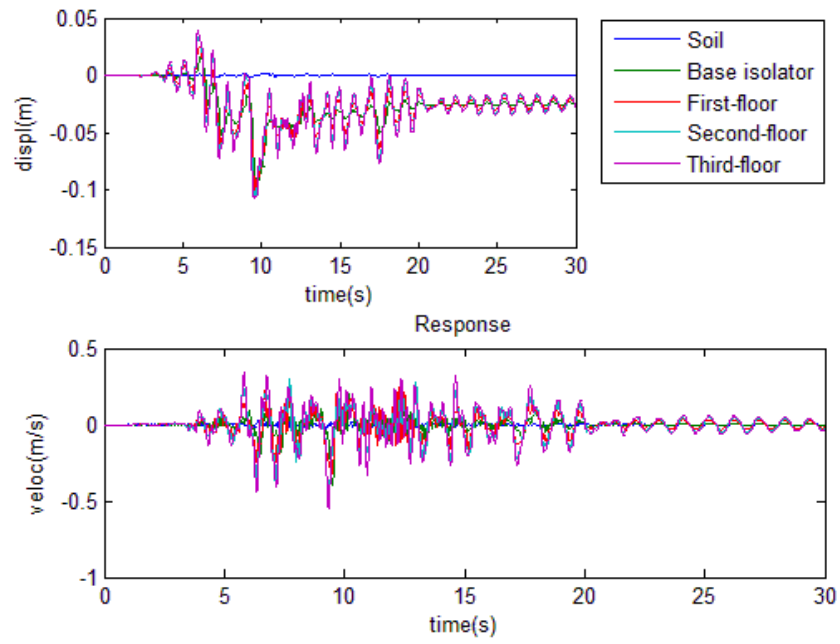


Figure 15: Displacement and velocity response for soil and each floor (Example 3).

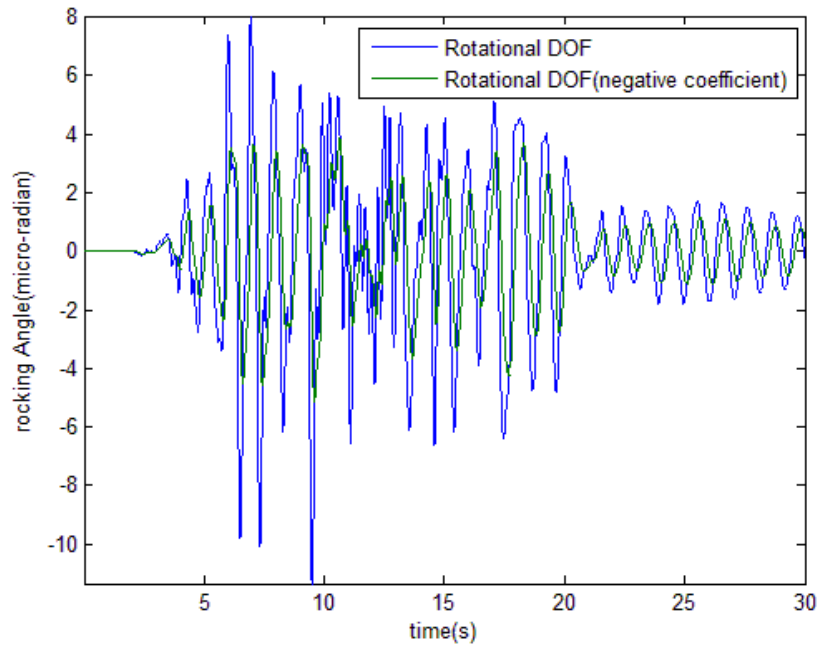
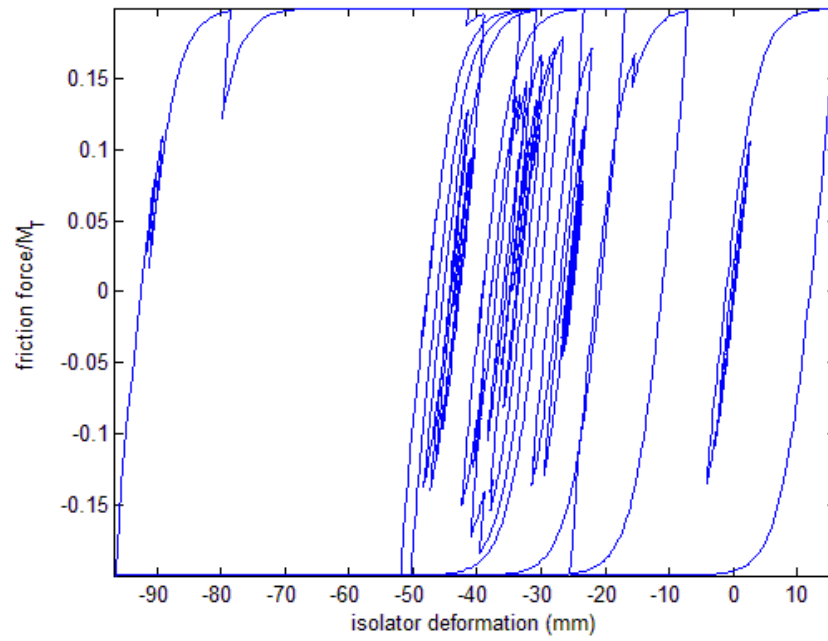
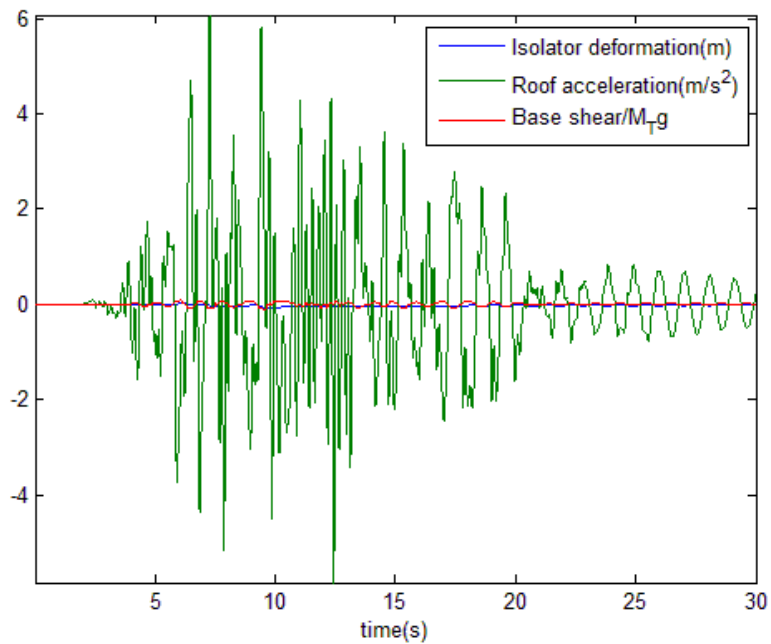


Figure 16: Two rocking degrees of freedom response (Example 3).



**Figure 17: Hysteresis loop (Example 3).**



**Figure 18: Base isolator deformation, roof acceleration, and base shear ratio. (Example 3)**

### 3.6 Discussion

Figure 4,9,14 plot the synthetic earthquake ground motion generated by passing Gaussian white noise through a 2<sup>nd</sup> order linear system and applying an envelope to the filtered process (Scruggs and Gavin 2010). The following table cited from Scruggs and Gavin’s controls handbook summarizes the input variables used to generate three different types of artificial earthquake ground motion, in the sense that the earthquake ground motion acceleration is modeled as an independent, enveloped and filtered white noise process. The earthquake ground motion for far field type is more stationary than record for near-fault type based on the evidence that far field ground motion record contains less cycles of motion. PGA and PGV denote the peak ground acceleration and

peak ground velocity respectively.  $\alpha$  is the envelope rise time parameter.  $\beta$  is envelope decay parameter, in s. Ground frequency and ground damping ratio are represented by  $f_g$  and  $z_g$  respectively. The values of two envelope parameters and two filter parameters are determined through fitting into the sets of ground acceleration records and to the spectral acceleration of the recorded acceleration ground motion respectively, and at the meantime, scale each record to match the specified PGV value of each type. The earthquake ground motion is sampled at uniformly spaced points in time, with a time step of 0.005 seconds.

**Table 11: Parameters values for earthquake ground motions**

Set	PGA	PGV	$\alpha$	$\beta$	$f_g$	$z_g$
FF	361	33	4.0	2.0	1.5	0.9
NFNP	537	52	3.0	2.0	1.3	1.1
NFP	525	80	1.0	2.0	0.5	1.8
	cm/s <sup>2</sup>	cm/s		s	Hz	-

Abbreviations: FF=far-field; NFNP=near-fault without pulse; and NFP=near-fault with pulse.

Due to the nonlinearity resulted from the frictional force, these differential equations are solved with a fourth order fixed time-step Runge-Kutta method. The earthquake acceleration is linearly interpolated in computing the state derivatives at times between the ground motion sample points.

Figures 5, 10, and 15 plot the displacements and velocities response of the soil, the base isolator, and the first floor, second floor and third floor respectively under the artificial earthquake ground motion. The soil deformation is very small compared to the

base isolator deformation and other floors' deformations regardless of the softness of the soil as well as the friction force. In comparison of figure 10 and 15, the isolator deflects dependently with the other floors when the friction force between the foundation and the first floor is small. However, for a large friction force between the foundation and the first floor, the peak base isolator deformation is much smaller compared to other floors. The peak deformation increases along the increase of the height. What's more, the base isolator and the floors above it didn't get back to the original position. A residual deformation was generated and remained. Additionally, for a higher floor, the peak velocity becomes larger.

The responses of the two rocking degrees of freedom,  $\Phi$  and  $\Phi_1$  are plotted in figures 6, 11 and 16. It is indicated that the rocking angle is very small, only up to ten micro radians. Also the rocking angle  $\Phi_1$  for the node which is connected with a spring and a dashpot of negative stiffness coefficient is smaller than the rocking angle  $\Phi$  for the node which is connected with a paralleled spring and dashpot.

Figures 7, 12 and 17 depict the hysteretic curve for the frictional force with respect to the base isolator deformation. For all of these three examples, the parameter  $r_y$  used to scale the isolator deformation rate is set to be 0.005m. Both in example 1 and example 2, the restoring frictional force is scaled by one percent of the total weight of the superstructure. In example 3, the restoring frictional force is scaled by twenty percent of the total weight of the superstructure.

The base isolator deformation, the roof acceleration and the base shear of the superstructure responses are summarized in figures 8, 13 and 18. Compare figure 8 with figure 4, and figure 13 with figure 9, the peak roof acceleration is smaller than the peak artificial earthquake ground acceleration. However, compare figure 18 with figure 14, the peak roof acceleration is larger than the peak artificial earthquake ground acceleration. This implies that a very large frictional force between the base isolator and the foundation may result in much larger maximum roof acceleration than expected.

## 4. Parameter Analysis

In order to investigate the effects of variability of the soil properties including the density, Poisson's ratio and the shear wave velocity, as well as the nonlinear effects of variability of the hysteretic frictional force between the foundation and first floor, three sets of parameter analysis were conducted in the following section. The only difference between these three examples are the types of synthetic earthquake ground motion.

### 4.1 Numerical Examples

In example 1, a far field earthquake ground motion is synthesized for the dynamic analysis of the whole system. An artificial earthquake ground motion representing a near-fault type of ground motion, without a pulse, is used in example 2. Example 3 also uses an artificial near-fault type of earthquake ground motion, but with pulse to carry out dynamic analyses.

Density, Poisson's ratio, and shear wave velocity are the main parameters to determine the stiffness of the soil. The shear wave velocity plays the most important role out of the three. Therefore, a range of soft soil conditions were modeled with different shear wave velocities ranging from 50 m/s to 200 m/s. The density of soil was selected from random samples of a log normal distribution with a median value of 1800 kg/m<sup>3</sup> and a coefficient of variance of 0.1. 1800 kg/m<sup>3</sup> is chosen to be used for modeling a typical sandy soil which is easily liquefied. Poisson's ratio was selected randomly from a range of 1/3 to 0.37. In addition, a range of isolator friction force values, ranging from 1

percent to 20 percent of the total superstructure weight was used to investigate this dynamic system. This resulted in 60 different soil stiffness-frictional force combinations. Each combination was simulated 100 times, and hence each time, 6000 simulations were subjected to one type of random earthquake. In total, 18000 simulations were generated for these three examples.

Other than these four key parameters, the remaining features were kept the same as the model calibrated in chapter three.

#### **4.1.1 Example 1: Synthetic far field earthquake ground motion**

In this example, 6000 simulations were conducted. The far field artificial earthquake ground motions were generated based on the parameter values from table 11. The results are summarized in figures 19-26. Figure 19 summarizes the peak deformation values for base isolator, in m and for low shear wave velocity to relatively high shear wave velocity. The y-axis is the maximum base-isolator deformation, while the x-axis represents the magnitude of the ratio between the frictional forces to the total weight of the superstructure. There is a strong correlation between the peak isolator deformation and the frictional force regardless of how low is the shear wave velocity of the soil. The peak deformation of isolator exponentially decays along the increase of the frictional force. Moreover, the decreasing rate also decreases when the frictional force becomes larger, which denotes that initially, the peak isolator deformation drops rapidly

for a small increase in friction. At larger values of the frictional force, however, the effect becomes less significant.

Figure 20 summarizes the plots of peak roof acceleration, in  $\text{m/s}^2$ . Similarly, the plots are for a range of shear wave velocities from lower than 180 m/s (soil class E) to higher than 180 m/s (soil class D). There is a strong relationship between the maximum roof acceleration and the frictional force as well. The peak roof acceleration increases logarithmically with the frictional force.

Figure 21 shows plots of base shear resulted from the superstructure, in ratio to total weight of the superstructure. Again, each plot represents a different shear wave velocity of the soil ranging from 50 m/s to 200 m/s. A linear line as a reference for the case when base shear equals to frictional force is plotted in each figure. It is clear that base shear is larger than each corresponding frictional force in all of these four plots, however, it approaches the frictional force asymptotically with the increase of frictional force. The reason for the relationship between the base shear and frictional force is relatively easy to see; other than the hysteretic frictional force between the foundation and the first floor, there exists a friction force between the bearing of isolator and the foundation. As the hysteretic frictional force increases, the effect of additional frictional force on the bearing deformation becomes less pronounced.

Figures 22-24 summarize the cumulative distribution of peak isolator deformations, peak roof accelerations and base shear with respect to various soil shear

wave velocities. They are plotted for the case when frictional force is 9 percent of the total weight of superstructure. The trend is not that obvious, however, it is expected that the peak isolator deformation as well as the base shear decreases along the increase of the shear wave velocity. The peak roof acceleration increases as the soil shear wave velocity increases.

Figure 25 plots the histogram of the peak isolator deformation for these 6000 simulations. The histogram can be seen as an empirical probability density function of the peak isolator deformation for far field earthquake ground motions. For this structural system, the peak isolator deformation during the far field earthquake concentrates mostly on the range between 0.025m to 0.1m. The maximum value of peak isolator deformation among these 6000 simulation is around 0.35m.

Figures 26 summarizes the residual deformations of the base isolator with respect to the hysteretic frictional force for various types of soil. As the hysteretic frictional force between the foundation and first floor increases, the residual deformation of the base isolator as well as the floors above increases. This implies that the base isolation system with large hysteretic frictional forces come to static equilibrium with larger residual deformations. The largest mean base isolator residual deformation is around 0.006 m occurring for a very soft soil.

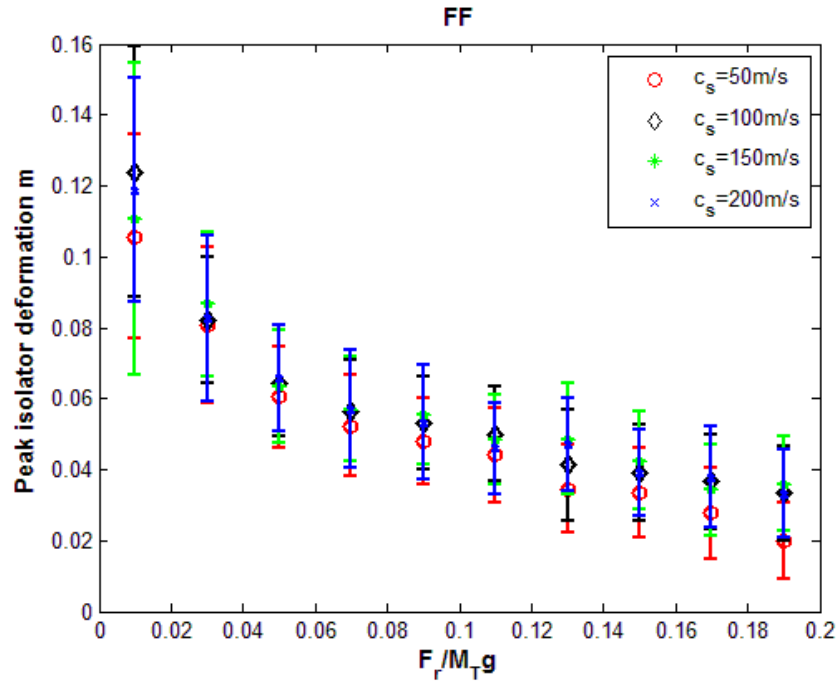


Figure 19: Peak isolator deformation vs. Frictional force (FF).

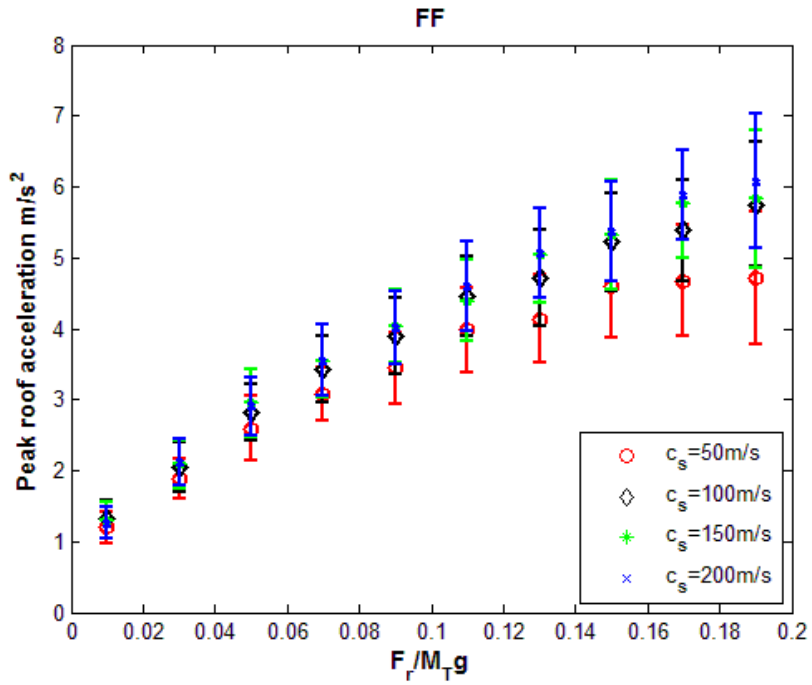


Figure 20: Peak roof acceleration vs. Frictional force (FF).

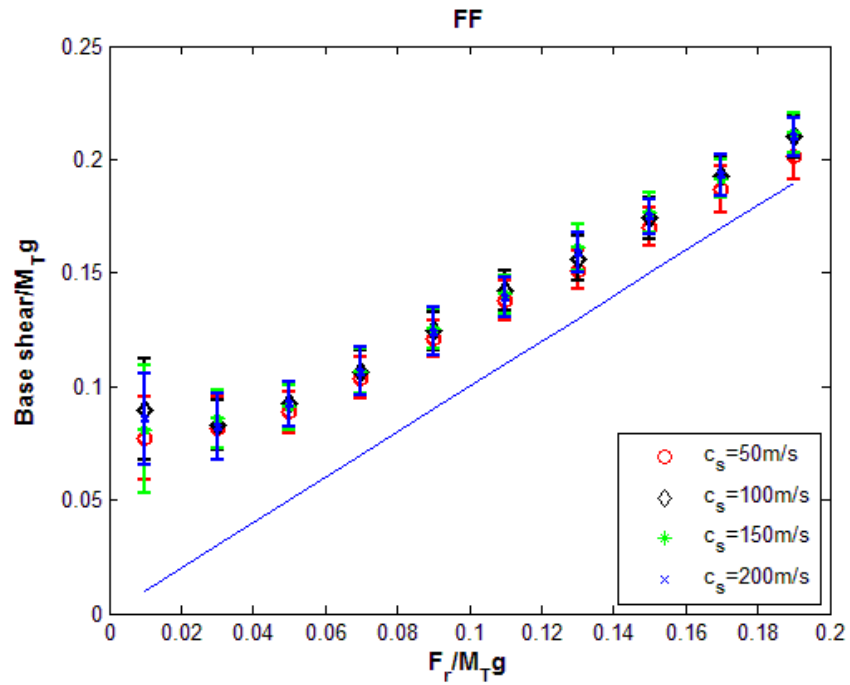


Figure 21: Base shear vs. Frictional force (FF).

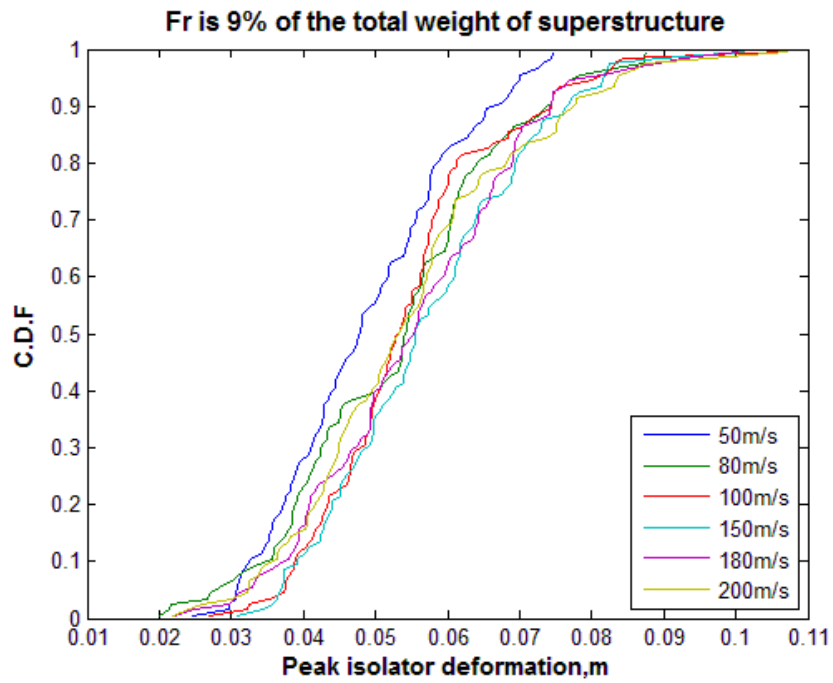


Figure 22: Peak isolator deformation empirical C.D.F (FF).

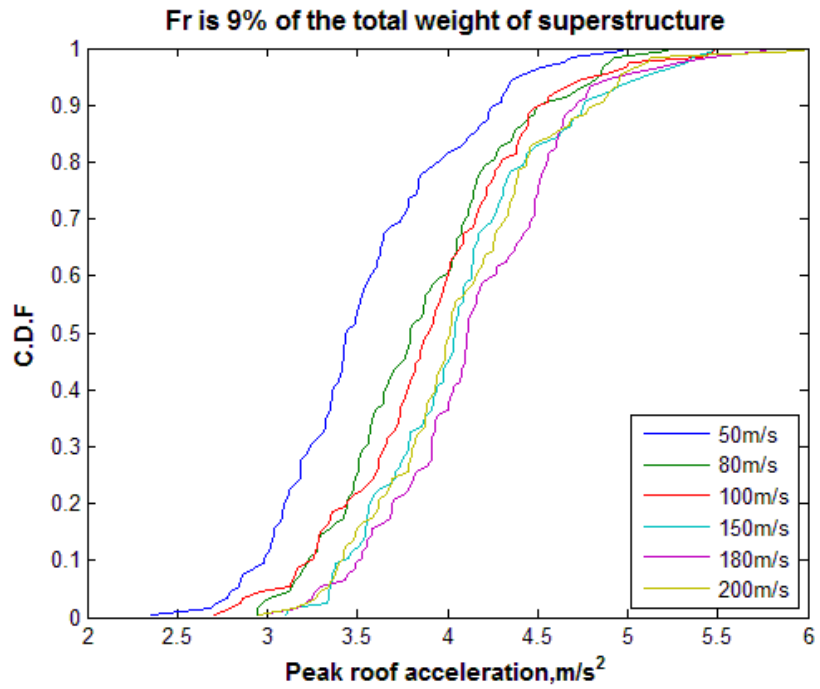


Figure 23: Peak roof acceleration empirical C.D.F (FF).

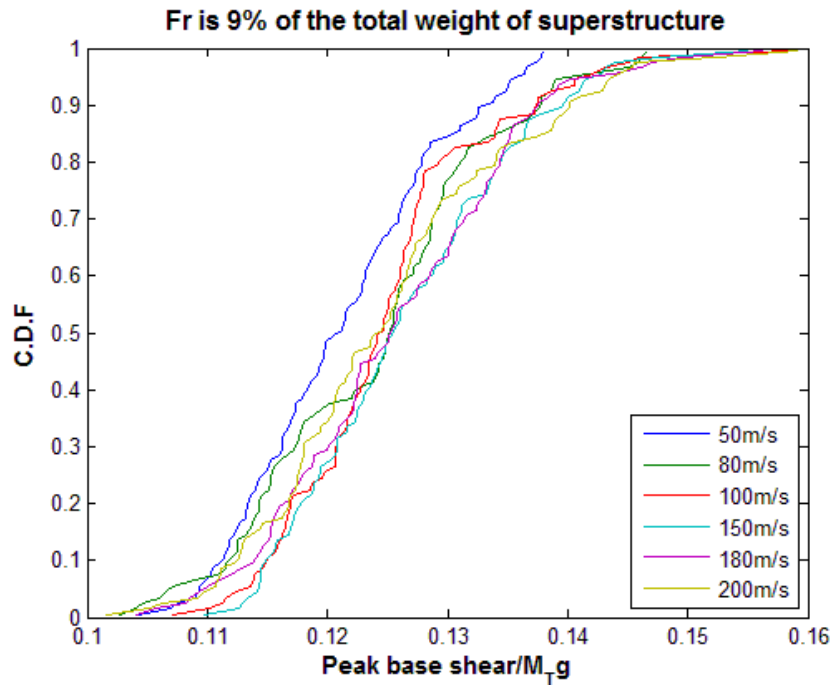


Figure 24: Peak normalized base shear empirical C.D.F (FF).

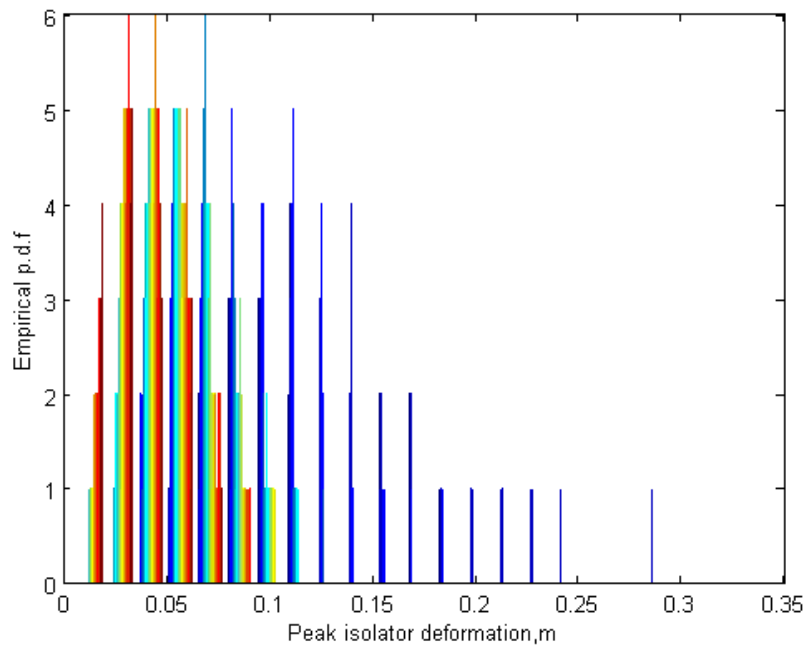


Figure 25: Peak isolator deformation empirical P.D.F, 6000 simulations (FF).

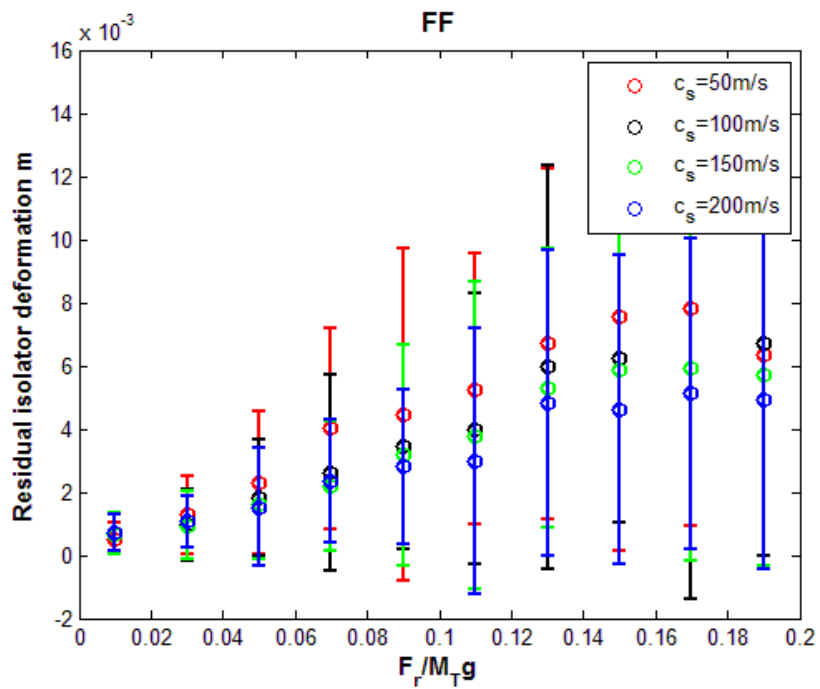


Figure 26: Residual base isolator deformation (FF).

#### **4.1.2 Example 2: Synthetic near field without pulse earthquake ground motion**

In this example, 6000 simulations were conducted. Ground motions corresponding to the near field sources but without a pulse were generated. The results are summarized in Figures 27-34.

Figure 33 shows that the peak isolator deformation of this system during the near-fault without pulse earthquake concentrates most on the range between 0.05m to 0.15m. The maximum value of peak isolator deformation among these 6000 simulation is around 0.45m.

Figure 34 summarizes the residual deformations of the base isolator with respect to the hysteretic frictional force for various types of soil. The largest mean base isolator residual deformation is around 0.011m occurring for the softest soil.

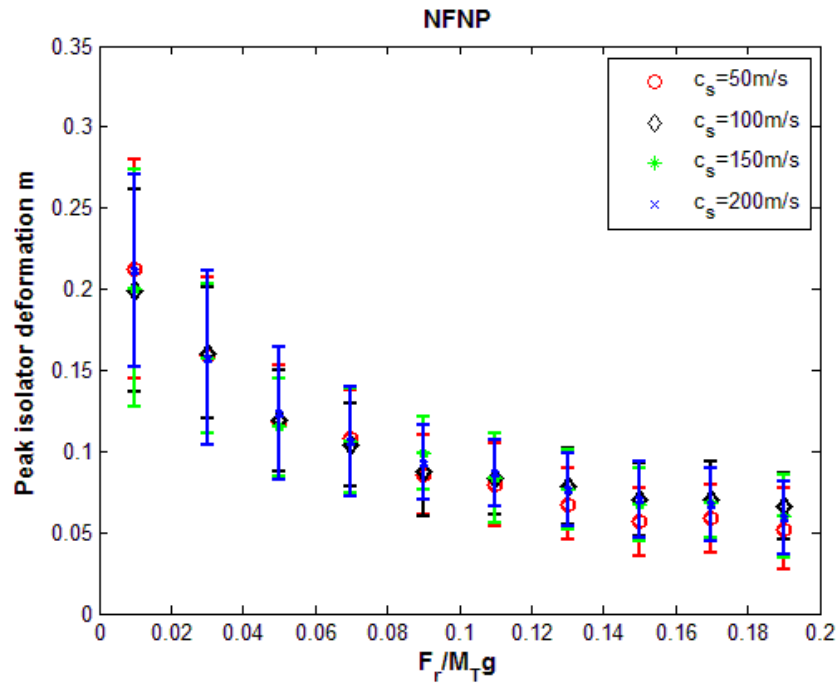


Figure 27: Peak isolator deformation vs. Frictional force (NFNP).

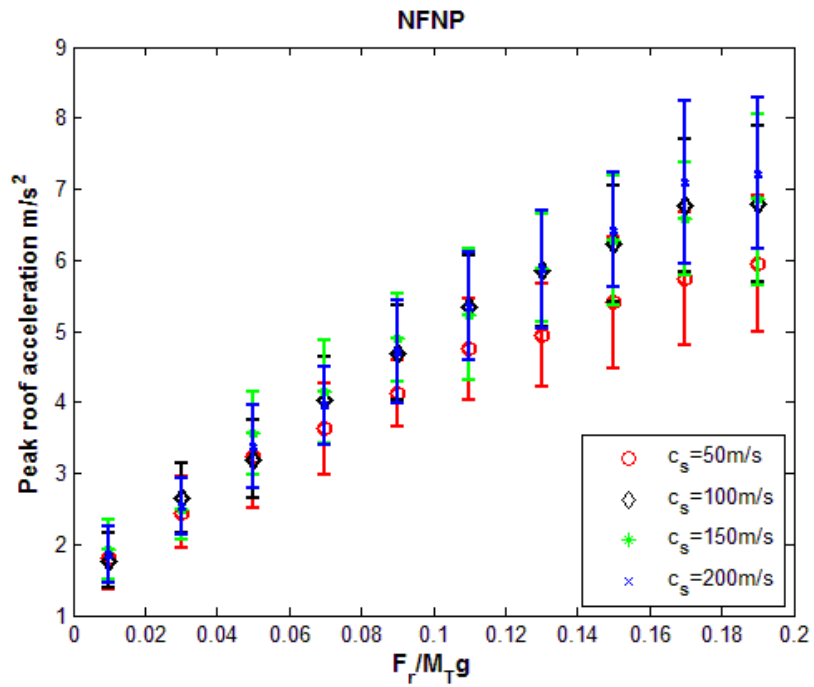


Figure 28: Peak roof acceleration vs. Frictional force (NFNP).

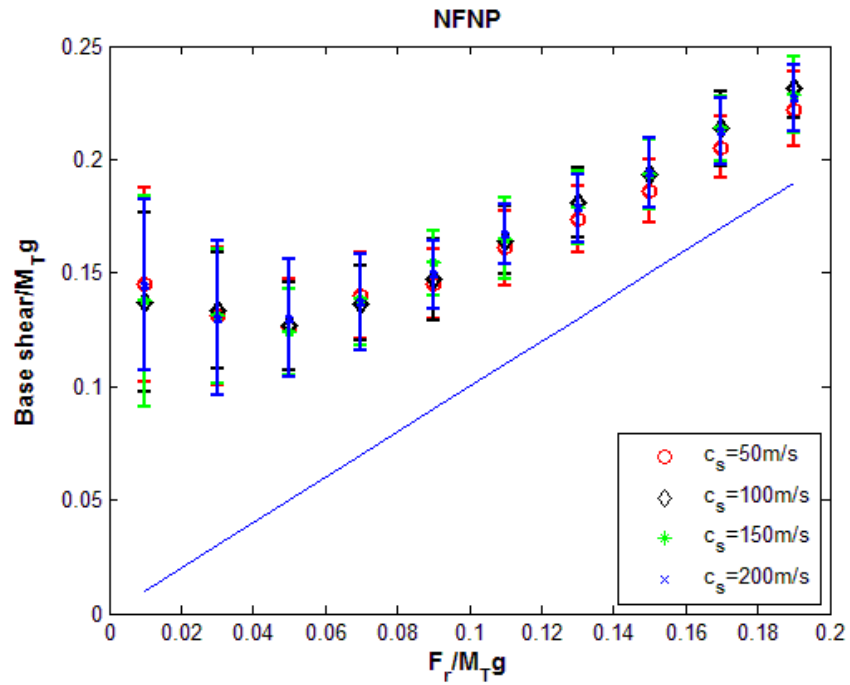


Figure 29: Base shear vs. Frictional force (NFNP).

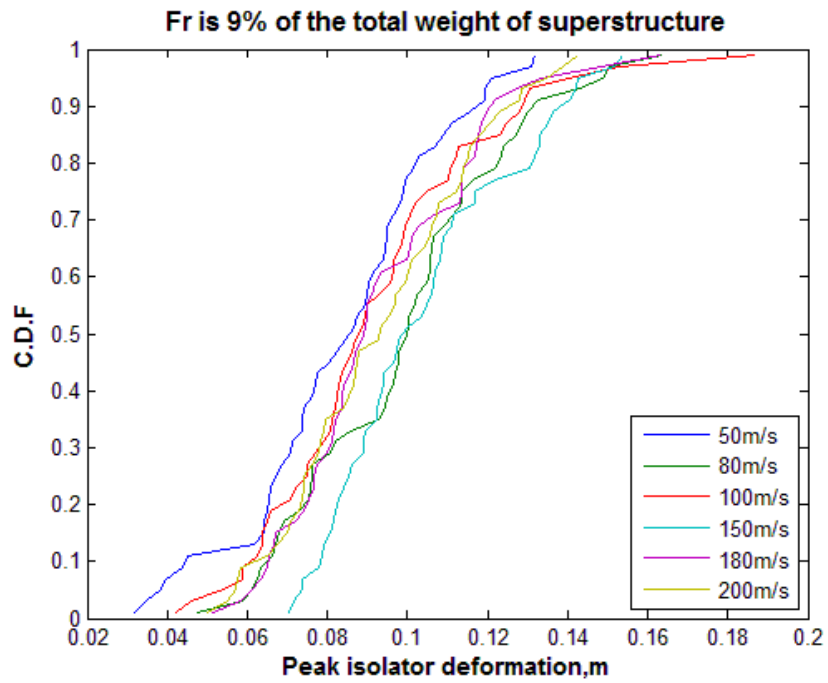


Figure 30: Peak isolator deformation empirical C.D.F (NFNP).

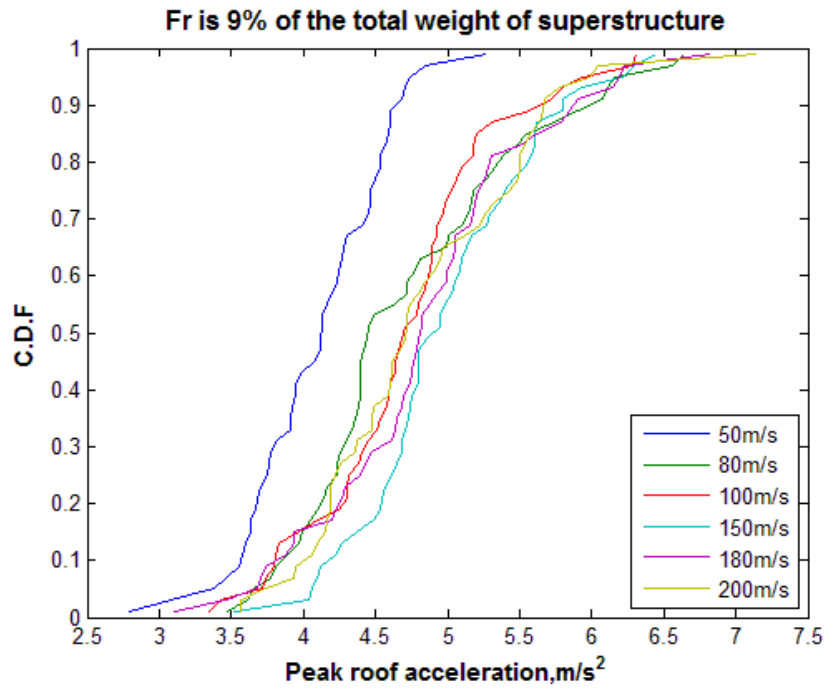


Figure 31: Peak roof acceleration empirical C.D.F (NFNP).

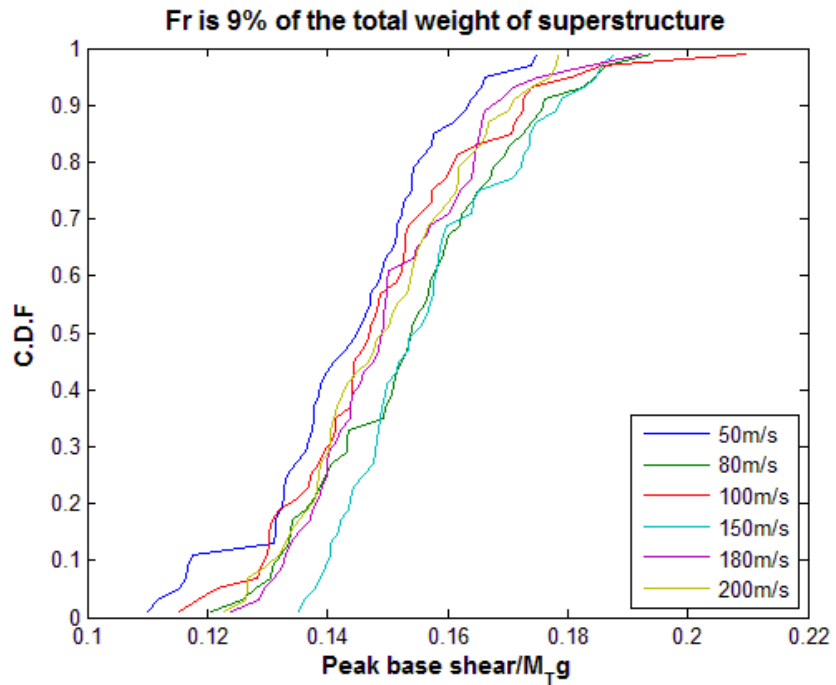


Figure 32: Peak normalized base shear empirical C.D.F (NFNP).

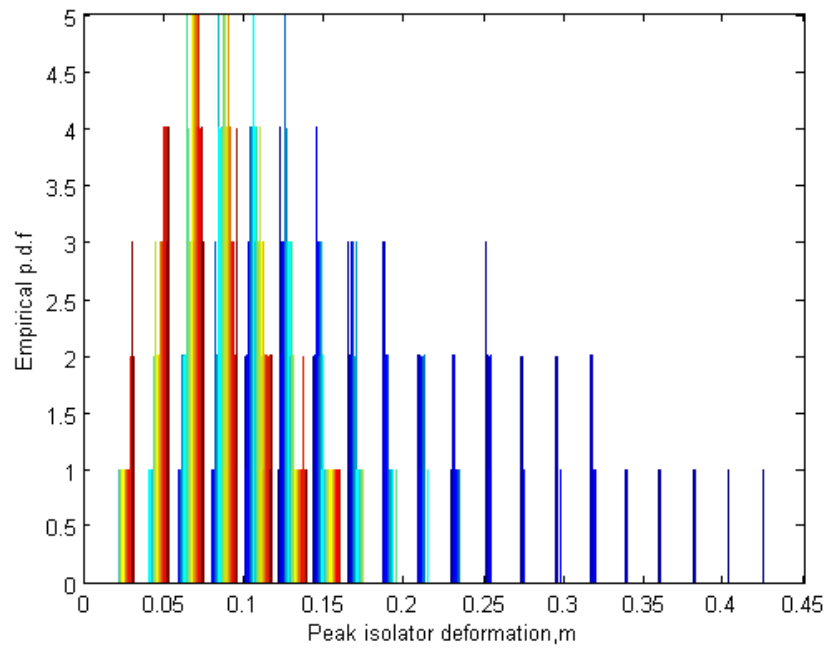


Figure 33: Peak isolator deformation empirical P.D.F, 6000 simulations (NFNP).

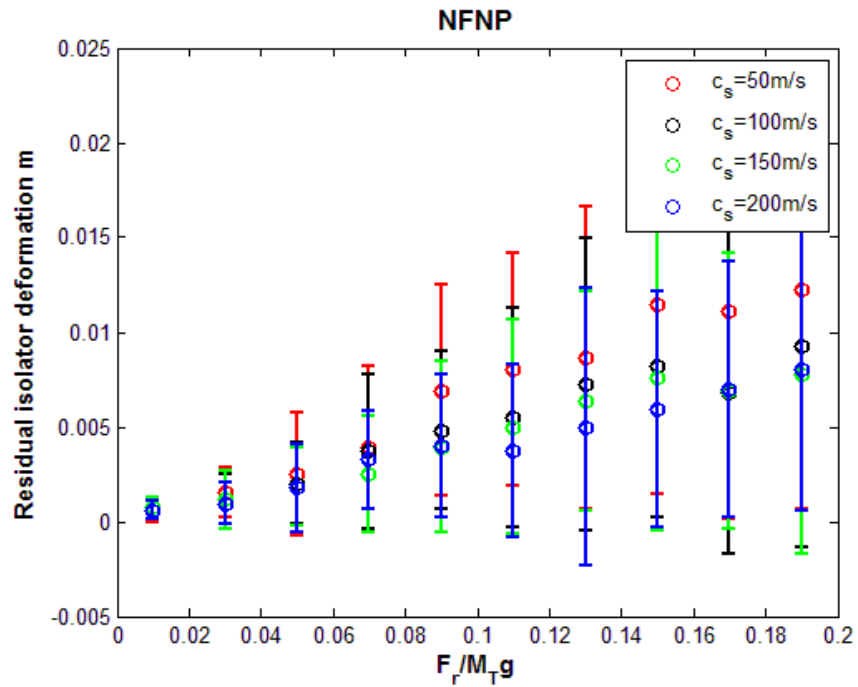


Figure 34: Residual base isolator deformation (NFNP).

### **4.1.3 Example 3: Synthetic near field with pulse earthquake ground motion**

In this example, 6000 simulations were conducted. Ground motions representative of near field earthquakes contain a pulse were generated. The results are summarized in Figures 35-42.

Figure 41 shows that the peak isolator deformation of this system during the near-fault with pulse ground motion concentrates most on the range between 0.05m to 0.25m. Moreover, in some simulations, the values reach out to around 0.8m.

Figure 42 summarizes the residual deformations of the base isolator with respect to the hysteretic frictional force for various types of soil. The largest mean base isolator residual deformation is around 0.015 m occurring for the softest soil.

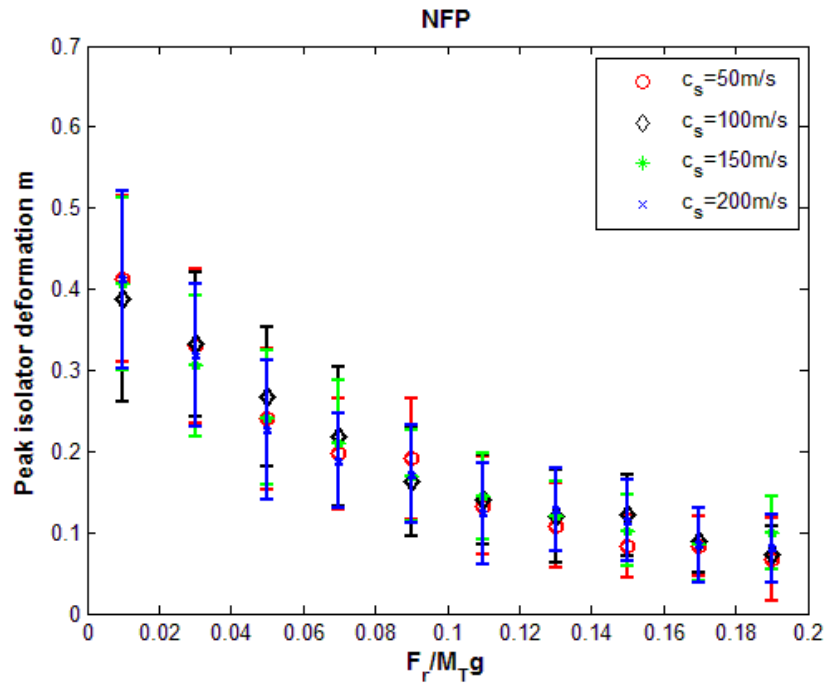


Figure 35: Peak isolator deformation vs. Frictional force (NFP).

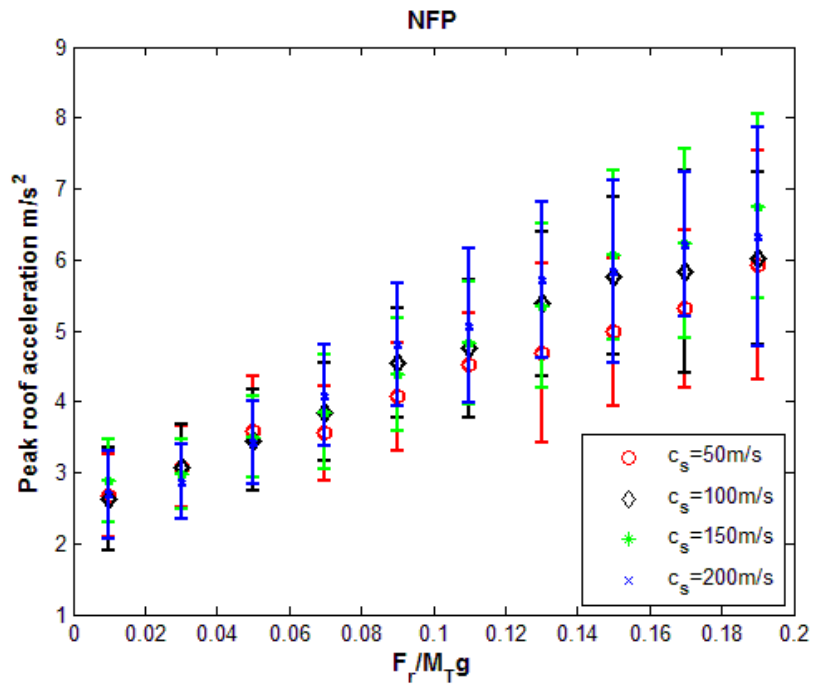


Figure 36: Peak roof acceleration vs. Frictional force (NFP).

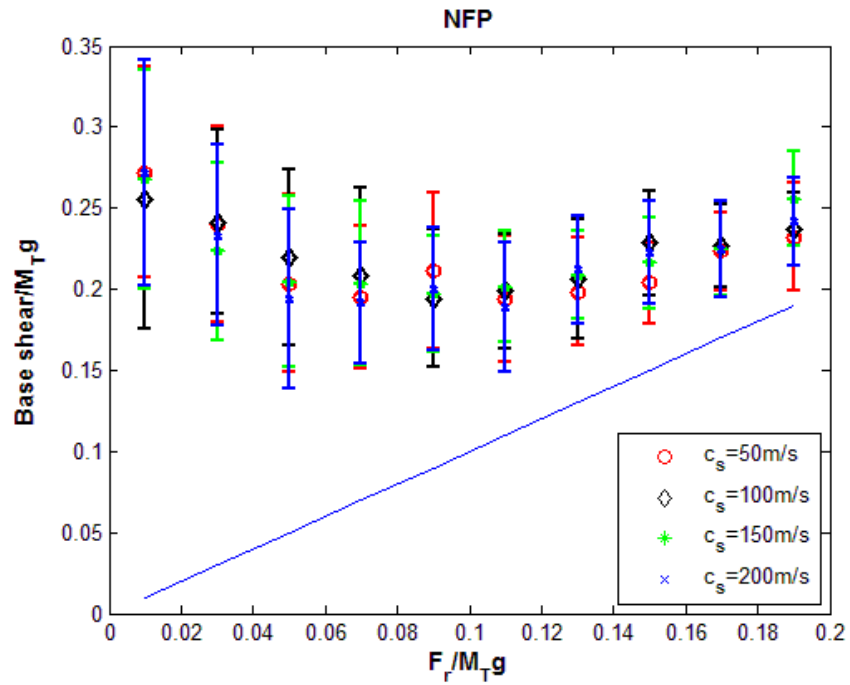


Figure 37: Base shear vs. Frictional force (NFP).

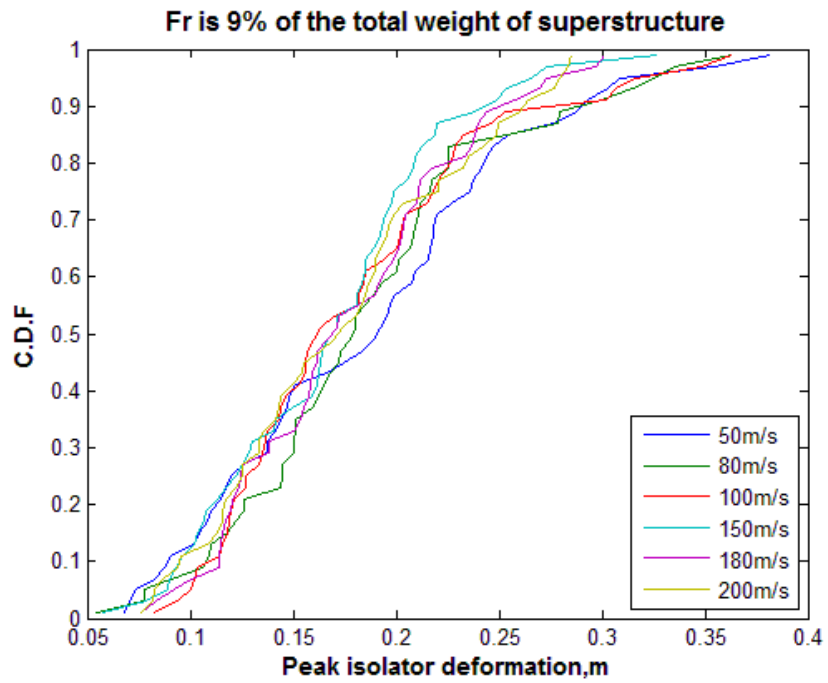


Figure 38: Peak base isolator deformation empirical C.D.F (NFP).

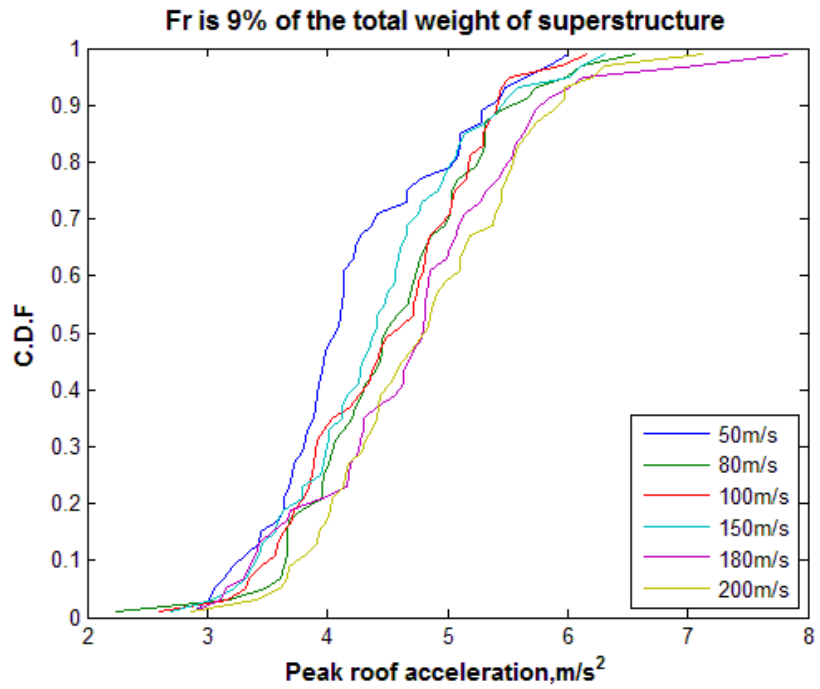


Figure 39: Peak roof acceleration empirical C.D.F (NFP).

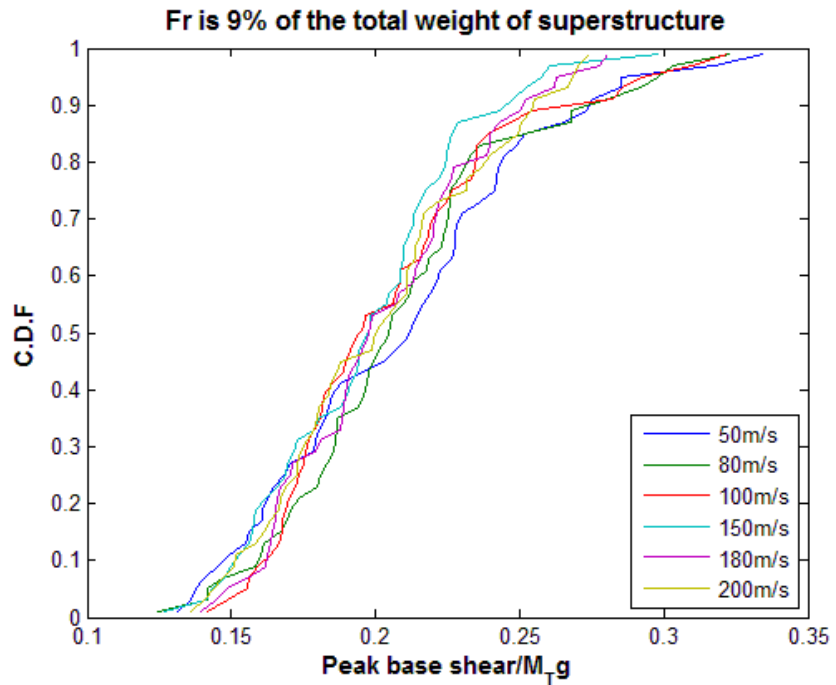


Figure 40: Peak normalized base shear empirical C.D.F (NFP).

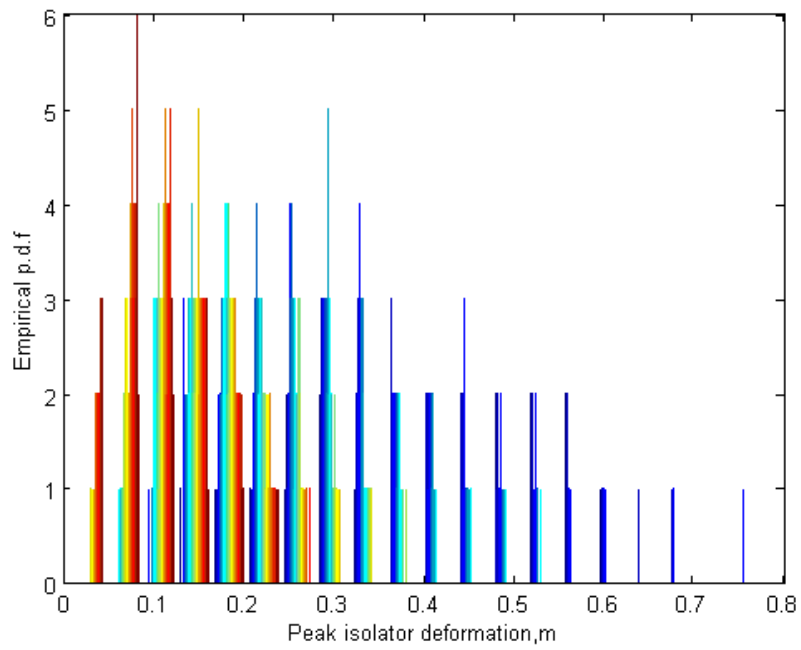


Figure 41: Peak isolator deformation empirical P.D.F, 6000 simulations (NFP).

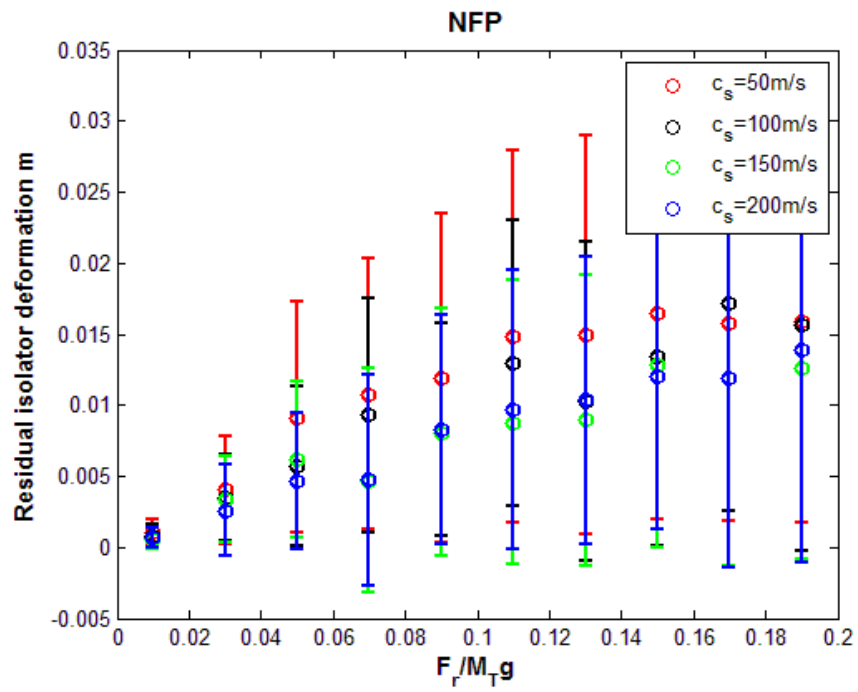


Figure 42: Residual base isolator deformation (NFP).

## 4.2 Discussion

Ideally, an effective base isolation system should achieve several objectives. An effective base isolation system should lengthen the system period to be longer than earthquake ground motion periods. An effective base isolation system should be able to accommodate large deformation domains. The isolation system should absorb and dissipate energy, through plastic deformation, friction, or viscous damping. Even though, it is not good to introduce too much damping of the system. The relationship between peak isolator deformation and frictional force obtained from the three numerical examples above show that the base isolation system with very high frictional force is actually less effective, in the sense that it increases the response of the superstructure. Furthermore, an effective base isolator should have small residual deformation after seismic attacks. In the parameter analysis, the residual deformation of the isolators becomes larger for a larger frictional force, which also implies that isolation systems with too large frictional force are less effective. Large friction forces couple the foundation to the first floor too strongly, forcing them deflect together and resulting in larger peak roof acceleration and smaller peak isolator deformation.

For this system, the artificial impulsive near field earthquake ground motion made the structure have larger peak isolator deformation and larger residual deformations of both base isolator and each floors. This mechanism implies that the near

field design should concern about the more severe impacts and more effective base isolation system.

Why are the trends of the peak isolator deformation, peak roof acceleration and base shear with respect to the shear wave velocity not obvious? In this study, the soil was idealized as a homogeneous linearly elastic, semi-infinite medium with mass density of  $\rho$  and was idealized as a semi-infinite elastic cone with an apex height of  $z_0$  for each coordinate of foundation motion. However, in reality, the soil is heterogeneous nonlinearly elasto-plastic. The stiffness of the soil, especially liquefied soil changes sensitively with respect to the loading history. Therefore, the modeling of the soil and description of its behavior will be difficult and are still being developed. In order to better display the nonlinear behaviors of liquefied soil, a stress-strain-dilatancy model developed by Misko Cubrinovski and Kenji Ishihara is adopted to be implemented into the OpenSees computational framework (Cubrinovski and Ishihara 1998). Then the base-isolated superstructure mounted on the liquefied soil can be better modeled though a finite element model in OpenSees.

## 5. Nonlinear Soil Modeling

A fully coupled effective stress method is the most competent approach in analyzing liquefaction problems, generally speaking, and in analyzing the response of saturated sand (Smith 1994). In particular, modified elasto-plastic models provide a reliable way of modeling sand behavior (Dafalias 1994). Cubrinovski and Ishihara's stress-strain-dilatancy soil model provides an alternative way of considering the effects of initial density and mean normal stress on sand behavior through considering state concept. Particularly, mean normal stress exhibits pronounced effects on the behavior of dense sand. As the confining stress increases, the behavior of dense sand become more contractive. Therefore, the change of characteristics of the stress-strain curve is distinct for dense sand. Whereas, for loose sand, the degree of influence of confining stress on its behavior is very low and the features of the stress-strain curve will remain almost unchanged. In the descriptions of Cubrinovski and Ishihara's stress-strain-dilatancy model, all stresses are effective stresses, compressive stresses and strains are taken to be positive as a convention. Both the effects of the initial density and confining stress on the elastic and plastic behavior are incorporated through state index  $I_s$ . The most distinctive features of the plasticity formulation shown in this model are the assumptions that sand continuously yields from the beginning of loading and that the direction of the plastic strain increment depends on the direction of the stress increment. This model adopts an associative flow rule.

## 5.1 Cubrinovski's soil model

The model presented in Cubrinovski and Ishihara's paper describes the plastic behavior through specifying a modified hyperbolic stress-strain relation and an energy based stress-dilatancy relation (Cubrinovski and Ishihara 1998).

In this model, a state index parameter  $I_s$  is used to link the relative initial state with the normalized stress-strain curve. Two characteristic states of sand are employed to define the state index  $I_s$ , the quasi steady state (QSS-line) and upper reference state (UR-line) (Cubrinovski and Ishihara 1998). The quasi steady state line is characteristic line representing the undrained shear behavior of sand and is represented by configurations on void ratio-effective confining stress plot. The quasi steady state is a transient steady state at which soil deforms without effective stress change or mitigation of pore water (Ishihara 1993).  $P_0$  represents the mean normal stress at which the threshold void ratio  $e_0$  line intersects the isotropic consolidation line of loosest state. If the initial confining stress  $P$  is smaller than  $P_0$ , the UR-line is a horizontal line corresponding to the threshold void ratio  $e_0$ , above which the initial state makes a zero strength at the steady state when undrained shearing is applied. If the initial confining stress  $P$  is larger than  $P_0$ , the isotropic consolidation line for the loosest state is used as UR-line. The threshold void ratio  $e_0$ , can be calculated as the point of the intersection between QSS-line and y-axis. Both shear and normal stresses are zeroes when the initial void ratio is larger than  $e_0$ .

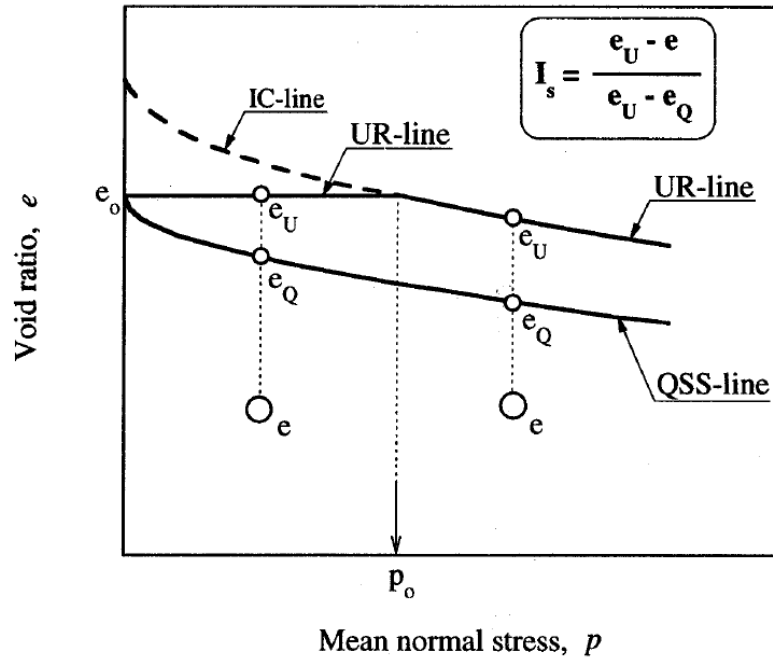


Figure 43: Definition of state index  $I_s$  (Ishihara 1993).

If an initial relative density and confining stress is given as  $(e, p)$ . The state index  $I_s$  is defined as in equation (5.1) by the ratio between the difference of the void ratio on the UR-line with the initial void ratio  $(e_U - e)$  and the difference of the void ratio on the UR-line with QSS-line  $(e_U - e_Q)$  at the initial confining stress.

$$I_s = \frac{e_U - e}{e_U - e_Q} \quad (5.1)$$

In Cubrinovski's model, the link between the state index  $I_s$  and the characteristics of the stress-strain curve were examined through a series of drained torsional  $p$ -constant tests on Toyoura sand samples. These tests give the evidence that initial states with similar state index have similar stress-strain curves, both the initial shear modulus and peak stress ratio decrease as the state index decreases until zero. The

stress ratio is the ratio between deviatoric stress  $q$  and hydrostatic stress  $p$ . It's worth pointing out that the initial state with a negative state index is taken as the characteristics of the state index of zero.

Furthermore, the experimental results from drained torsional  $p$ -constant tests demonstrate that there exists a linear relation between the peak stress ratio, the maximum initial plastic shear modulus, the minimum initial plastic shear moduli, and the state index  $I_S$ .

$$\left(\frac{q}{p}\right)_{max} = a1 + b1I_S \quad (5.2)$$

$$G_{N,max} = a2 + b2I_S \quad (5.3)$$

$$G_{N,min} = a3 + b3I_S \quad (5.4)$$

The modified hyperbolic relation is formulated as in equation (5.5) between the stress ratio  $q/p$  and the plastic shear strain  $\varepsilon_q^p$ , together with the normalized initial shear modulus  $G_N$  both counted in the denominator and numerator.

$$\frac{q}{p} = \frac{G_N \varepsilon_q^p \left(\frac{q}{p}\right)_{max}}{\left(\frac{q}{p}\right)_{max} + G_N \varepsilon_q^p} \quad (5.5)$$

$$G_N = (G_{N,max} - G_{N,min}) \exp\left(-f \frac{\varepsilon_q^p}{\varepsilon_q^0}\right) + G_{N,min} \quad (5.6)$$

The normalized initial shear modulus  $G_N$  degrade exponentially from  $G_{N,max}$  to  $G_{N,min}$  along the increase of plastic shear strain as is shown in Figure 44. In equation (5.6),  $\varepsilon_q^0$  is assumed to be fixed at 0.01. The degradation constant is denoted by  $f$ .

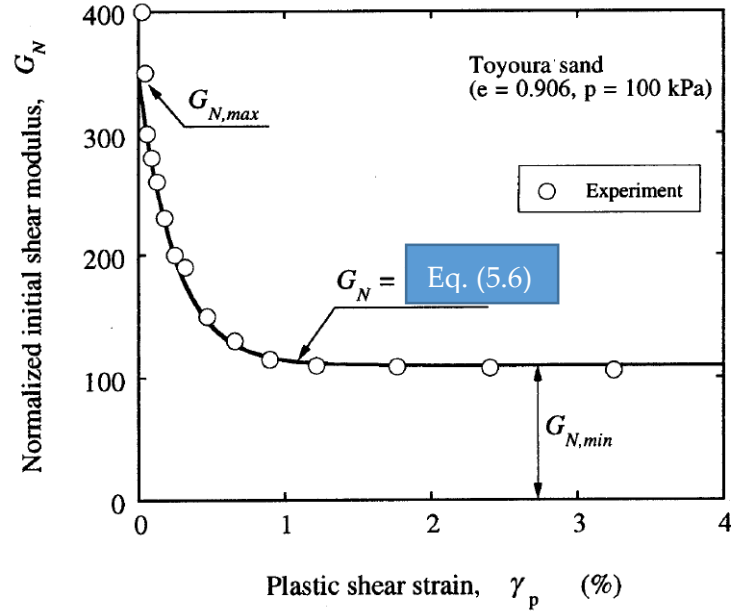


**Figure 44: Degradation of normalized initial shear modulus vs. shear strain (Cubrinovski and Ishihara 1998).**

Along the loading history, the state of the void ratio  $e$  and confining stress  $p$  changes, which implies that the state index changes continuously. The current state index  $I_s$ , then is determined through replacing  $e_U$  and  $e_Q$  by the void ratios of the UR-line and QSS-line at the current mean normal stress  $p$ .

Another particular energy based stress-dilatancy relation (Roscoe et al. 1963) is used in this constitutive model. The relation links the ratio between the plastic volumetric strain increment and the shear strain increment with the rate  $\mu$  at which the energy  $W$  is dissipated and the stress ratio  $q/p$ .  $c$  is a non-coaxiality term.

$$\frac{d\varepsilon_v^p}{d\varepsilon_q^p} = \mu - \frac{q}{p} c \quad (5.7)$$

The experiments show the evidence that the rate  $\mu$  during the shear distortion of a unit volume soil increases as the increase of the plastic shear strain as is shown in equation (5.8). It is assumed that in this stress-dilatancy relation,  $\mu_0$ , the slope of the normalized shear work with respect to plastic shear strain curve at small strains;  $M$ , the slope of the normalized shear work with respect to plastic shear strain curve at large strains;  $S_C$ , the dilatancy parameter are independent of both initial void ratio and confining stress.

$$\mu = \mu_0 + \frac{2}{\pi}(M - \mu_0)\tan^{-1}\left(\frac{\varepsilon_q^p}{S_C}\right) \quad (5.8)$$

The influence of the initial state index is incorporated into the relation through the rate  $\mu$ . It is worth mentioning that the dilatancy parameter  $S_C$  specifies the shear strain at which the rate is equal to half of the sum of  $\mu_0$  and  $M$ .  $S_C$  controls the pore pressure development and is determined through simulating a given cyclic strength with respect to number of cycles curve which embeds liquefaction effect into the constitutive model. The incremental formulation and plasticity formulation are specifically discussed both for monotonic loading and cyclic loading which embody the essence of the stress-strain-dilatancy into the elasto-plastic model.

A cogent comparison between experimental tests and numerical simulations of Toyoura Sand is conducted in Cubrinovski and Ishihara's paper. The effective stress paths and the stress-strain curves for various void ratios of dry-pluviated Toyoura sand are close with each other respectively for both results obtained from numerical

simulations and from torsional simple shear tests. This implies that through both considering the state concept and the modified elasto-plasticity into this framework, the sand behavior is successfully captured over a wide range of initial void ratio and confining stress. Moreover, the constitutive model presented in his paper is practical in analyzing liquefaction problem because only a single set of material parameters is needed to model the sand behavior.

## 5.2 2D plasticity formulation

Given a current stress vector and a strain increment vector, then use the engineering shear strain definition and formulate the model in  $X - Y - p$  space.

$$X = \frac{1}{2}(\sigma_y - \sigma_x) \quad (5.9)$$

$$Y = \tau_{xy} \quad (5.10)$$

$$p = \frac{1}{2}(\sigma_y + \sigma_x) \quad (5.11)$$

$$q = \sqrt{X^2 + Y^2} \quad (5.12)$$

$$\eta = \frac{q}{p} \quad (5.13)$$

$$d\varepsilon_v^p = d\varepsilon_x^p + d\varepsilon_y^p \quad (5.14)$$

$$d\varepsilon_q^p = \sqrt{(d\varepsilon_y^p - d\varepsilon_x^p)^2 + (d\gamma_{xy}^p)^2} \quad (5.15)$$

The total strain increment can be decomposed into two parts including an elastic part and a plastic part.

$$d\varepsilon_{ij} = d\varepsilon_{ij}^e + d\varepsilon_{ij}^p \quad (5.16)$$

The elastic incremental relation is given by equation (5.17).

$$d\sigma_{ij} = E_{ijkl}d\varepsilon_{kl}^e \quad (5.17)$$

The increment of the plastic strain is described in equation (5.18)

$$d\varepsilon_{ij}^p = \langle L \rangle \frac{\partial g}{\partial \sigma_{ij}} \quad (5.18)$$

$$\langle L \rangle = 0 \text{ for } L \leq 0$$

$$\langle L \rangle = L \text{ for } L > 0$$

$$L = \frac{1}{H_p} \frac{\partial l}{\partial \sigma_{ij}} d\sigma_{ij} \quad (5.19)$$

As is expressed in equation (5.19),  $L$  is the loading index which measures the magnitude of the plastic strain increment.  $H_p$  represents the plastic modulus that is a constant along the loading surface. The plastic potential is expressed as  $g$  in equation (5.18).

The failure surface is described in equation (5.20).

$$f = \{X^2 + Y^2\}^{1/2} - \eta_{max}p = 0 \quad (5.20)$$

$\eta_{max}p$  represents the radius of the failure circle.

To find the conjugate stress point  $(X_c, Y_c)$  of current state stress point  $(X, Y)$  using equations (5.21), (5.22) and geometric relations.

$$\{X_c^2 + Y_c^2\}^{1/2} - \eta_{max}p = 0 \quad (5.21)$$

$$Y_c = (X_c - X)\tan 2\xi + Y \quad (5.22)$$

At the conjugate stress point  $(X_c, Y_c)$ ,  $\frac{\partial g}{\partial \sigma_{ij}}$  is replaced by  $\frac{\partial f}{\partial \sigma_{ij}}$

$$d\varepsilon_y^p - d\varepsilon_x^p = L \left( \frac{\partial f}{\partial X} \right)_{X=X_c, Y=Y_c} = L \frac{Xc}{\eta_{max}^p} \quad (5.23)$$

$$d\gamma_{xy}^p = L \left( \frac{\partial f}{\partial Y} \right)_{X=X_c, Y=Y_c} = L \frac{Yc}{\eta_{max}^p} \quad (5.24)$$

Substituting (5.23) and (5.24) into (5.15)

$$d\varepsilon_q^p = L \quad (5.25)$$

And substituting (5.14) and (5.15) and (5.25) into (5.7)

$$\frac{d\varepsilon_y^p + d\varepsilon_x^p}{L} = \mu - \eta c \quad (5.26)$$

$$c = \cos 2\varphi$$

$$\varphi = |\alpha - \beta|$$

$\varphi$  is an angle between the direction of the principal stress and the direction of the plastic strain increment as is shown in figure 79.

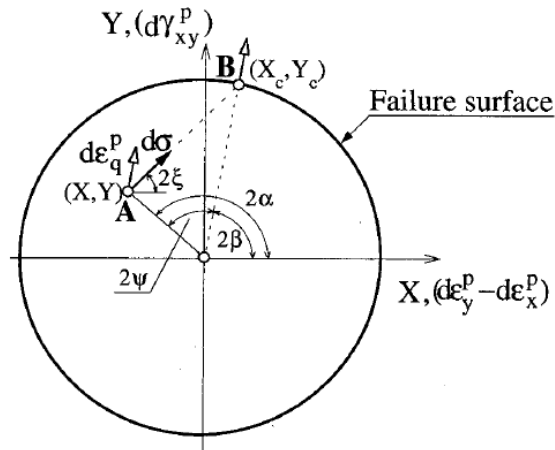


**Figure 45: Flow rule (Gutierrez et al., 1993).**

Combining (5.23) (5.24) and (5.26), the plastic strain increment vector is obtained

$$\begin{aligned}
d\varepsilon_x^p &= \frac{L}{2} \left\{ \mu - \eta c - \frac{Xc}{\eta_{max} p} \right\} \\
d\varepsilon_y^p &= \frac{L}{2} \left\{ \mu - \eta c + \frac{Xc}{\eta_{max} p} \right\} \\
d\gamma_{xy}^p &= L \frac{Yc}{\eta_{max} p}
\end{aligned} \tag{5.27}$$

In addition, the loading surface is expressed in equation (5.28) and is shown in figure 80.

$$\begin{aligned}
l &= q - \eta p = 0 \\
&= l\{\sigma_{ij}, \eta(\varepsilon_q^p)\}
\end{aligned} \tag{5.28}$$

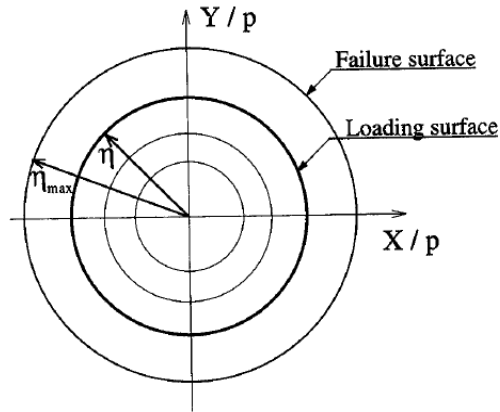


**Figure 46: Size of loading surface and failure surface (Cubrinovski and Ishihara 1998).**

For a stress increment  $d\sigma_{ij}$  directed outward the loading surface, the new stress state should remain on the loading surface,

$$dl = \frac{\partial l}{\partial \sigma_{ij}} d\sigma_{ij} + \frac{\partial l}{\partial \eta} \frac{\partial \eta}{\partial \varepsilon_q^p} d\varepsilon_q^p \tag{5.29}$$

$$= LH_p + \frac{\partial l}{\partial \eta} \frac{\partial \eta}{\partial \varepsilon_q^p} L = 0$$

$$H_p = - \frac{\partial l}{\partial \eta} \frac{\partial \eta}{\partial \varepsilon_q^p} \tag{5.30}$$

Take the derivatives of  $l$  and  $\eta$ , then substitute into equation (5.30).

$$H_p = \{G_N - f \frac{\varepsilon_q^p}{0.01} (G_N - G_{N,min})\} p \{1 - \frac{\eta}{\eta_{max}}\}^2 \quad (5.31)$$

$$H_p = \begin{cases} G_{max} & \text{at } \varepsilon_q^p = 0 \\ 0 & \text{at } \varepsilon_q^p \rightarrow \infty \end{cases}$$

The yield direction is now defined by the normal to the failure surface at the conjugate stress point  $(X_c, Y_c)$  as is presented in equation (5.32) and the loading index  $L$  could be calculated as is shown in equation (5.33).

$$\frac{\partial l}{\partial X} = (\frac{\partial f}{\partial X})_{X=X_c, Y=Y_c}, \frac{\partial l}{\partial Y} = (\frac{\partial f}{\partial Y})_{X=X_c, Y=Y_c} \quad (5.32)$$

$$L = \frac{1}{H_p} \left\{ \frac{1}{2} \left[ -\frac{q}{p} - \frac{X_c}{\eta_{max} p} \right] d\sigma_x + \frac{1}{2} \left[ -\frac{q}{p} - \frac{X_c}{\eta_{max} p} \right] d\sigma_y + \frac{Y_c}{\eta_{max} p} d\tau_{xy} \right\} \quad (5.33)$$

## 6. OpenSees Simulation

OpenSees (Open system for earthquake engineering simulation) is an object-oriented open source software which allows users to implement finite element methods to model the structural and geotechnical systems and simulate the response under earthquake loading. It has been under development by the Pacific Earthquake Engineering Research Center since 1997. Because OpenSees is an object-oriented framework software, in a finite element application, mainly four types of objects, model builder object, domain object, recorder object and analysis object need to be constructed. In OpenSees, the interpretation is accomplished by adding commands into Tcl script for finite element analysis. Each command is associated with a C++ procedure that is built inside and is called by the interpreter to analyze the command (Mazzoni et. al 2006).

Why is OpenSees chosen in this study? Several reasons are given as follows. To begin with, it is an open source which is free to be used. Second, both linear and nonlinear structural and geotechnical models can be built in OpenSees. Third, various simulations: static push-over analysis, static reversed-cyclic analysis, dynamic time-series analysis, uniform-support excitation, multi-support excitation can be effectively conducted. Last but not the least, OpenSees provides a library of various materials, elements and analysis which is powerful for numerical simulation of nonlinear systems.

However, since OpenSees is a research-developed software which denotes that it is not maturely developed, the simulations conducted using OpenSees need to be testified with results obtained from other software.

## 6.1 UCSD Soil Model

Our collaborators in New Zealand are developing the code for the implementation of Cubrinovski's soil model in OpenSees, in the meantime, we can explore an existing nonlinear soil model that have been developed in OpenSees by researchers from University of California, San Diego. Particularly, nonlinear undrained soil response under cyclic loading condition can be effectively simulated. Generally speaking, there are two ways to simulate pressure sensitive soil response under fully undrained condition in OpenSees using UCSD soil model. Either embed a PressureDependMultiYield material into FluidSolidPorousMaterial or use PressureDependMultiYield material with one of the solid-fluid fully coupled elements with very low permeability. The material needs to be used with a solid-fully coupled elements with appropriate permeability values in order to simulate partially drained soil response. In addition, during the gravity loading stage, the material has linear elastic behavior, however, during the dynamic loading stage, the material behavior becomes elasto-plastic. The dilatancy effect is a contraction or dilation effect of the volume induced by the shear strain which is produced using a non-associative flow rule in this model. In UCSD soil model, the plasticity is formulated based on the multi surface

concepts and the yielding surface uses Drucker-Prager type. A non-associative flow rule is adopted. In order to better understand the elasto-plastic framework for UCSD soil model in OpenSees. A column of 2D four node plane strain element using bilinear isoparametric formulation for saturated, undrained pressure dependent material modeling is repeated (Yang, et al 2003).

The example system is subjected to 1D sinusoidal base shaking. The soil column is composed of 10 elements and is 10 meters in depth. The base of the soil column is fixed and the surface of the soil column is set as a free drainage surface. The property parameters are chosen to be representatives for loose sand.

Figures 47-52 summarize the plots of the modeled soil column subjected to a sinusoidal base shaking. Figure 47 plots the lateral displacement of the soil element at different depth. As can be seen, the soil element that is more close to surface has larger lateral displacement during the cyclic loading application. Figure 48 plots the lateral acceleration of the soil element at different depth. Figures 49-51 plot the shear stress-strain curve and effective stress path. The nonlinear behavior is clearly evident. Figure 52 plots the excess pore water pressure build-up in time-scale and in space-scale.

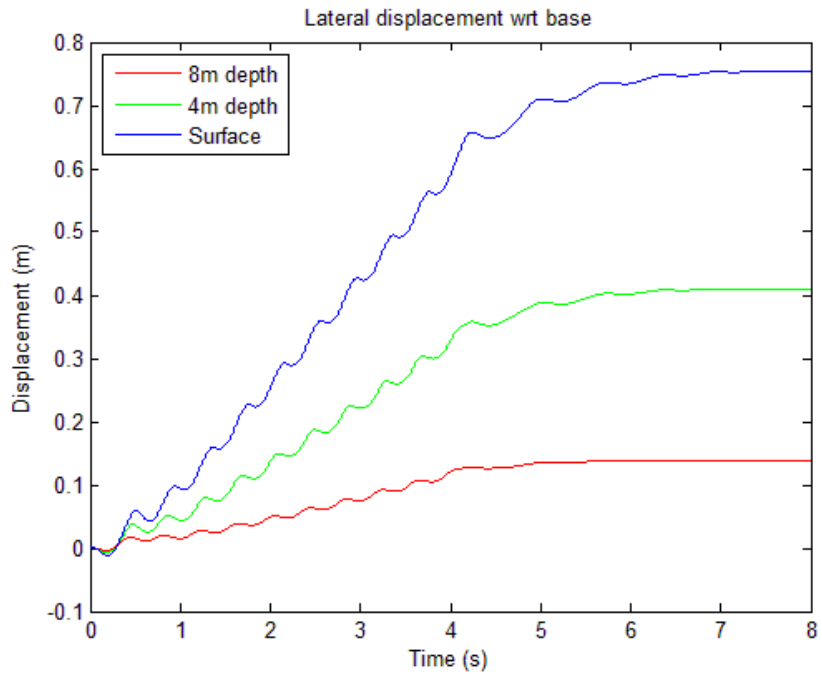


Figure 47: Lateral displacement for soil element at different depth.

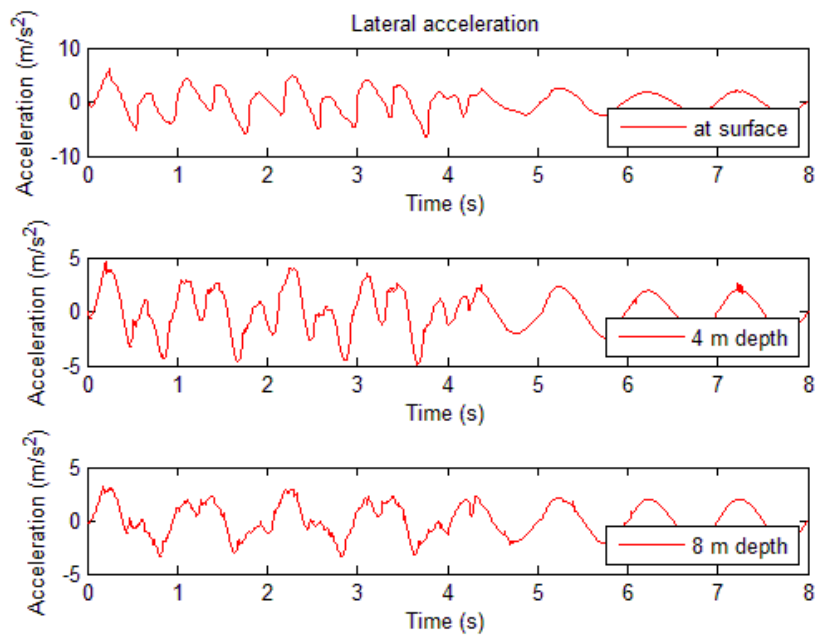
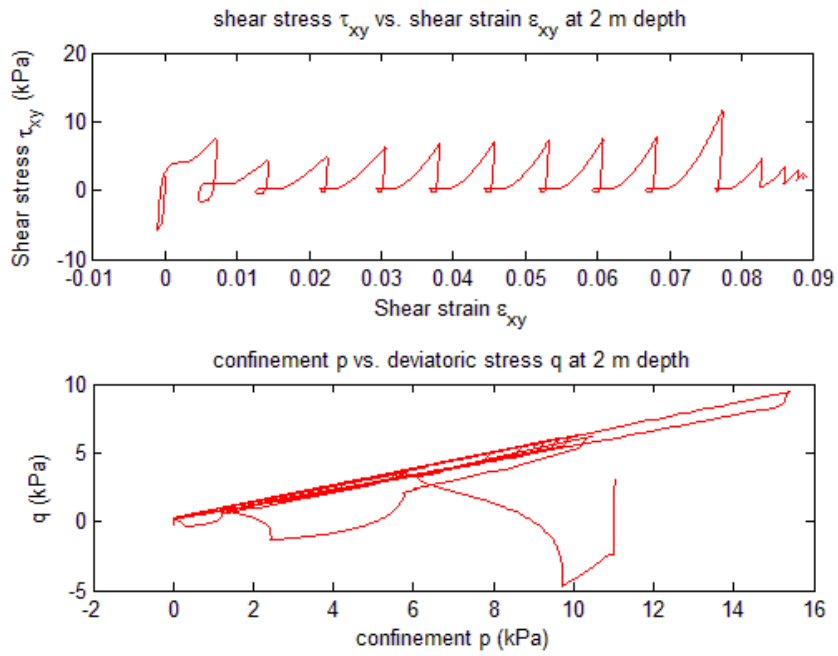
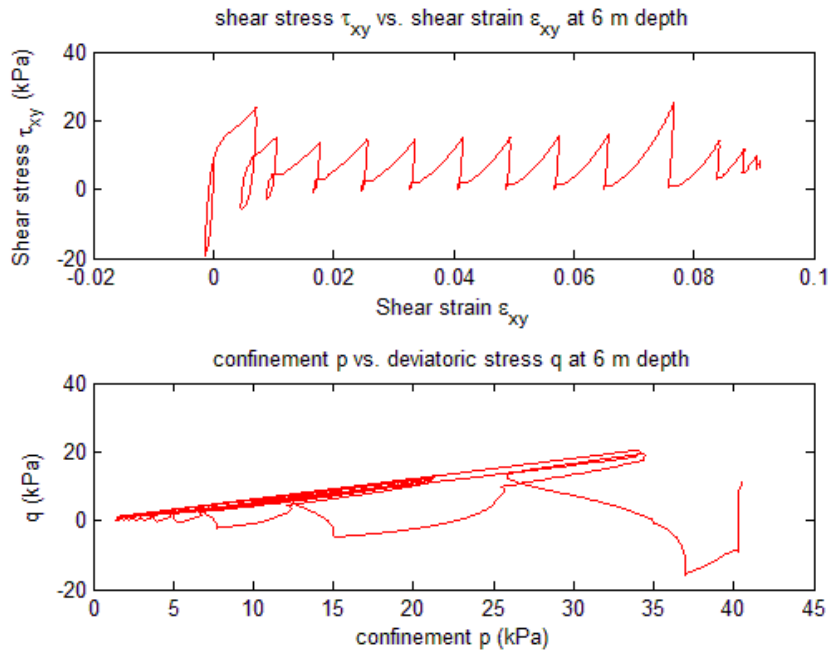


Figure 48: Lateral acceleration for soil element at different depth.



**Figure 49: Stress-strain output at 2 m depth.**



**Figure 50: Stress-strain output at 6 m depth.**

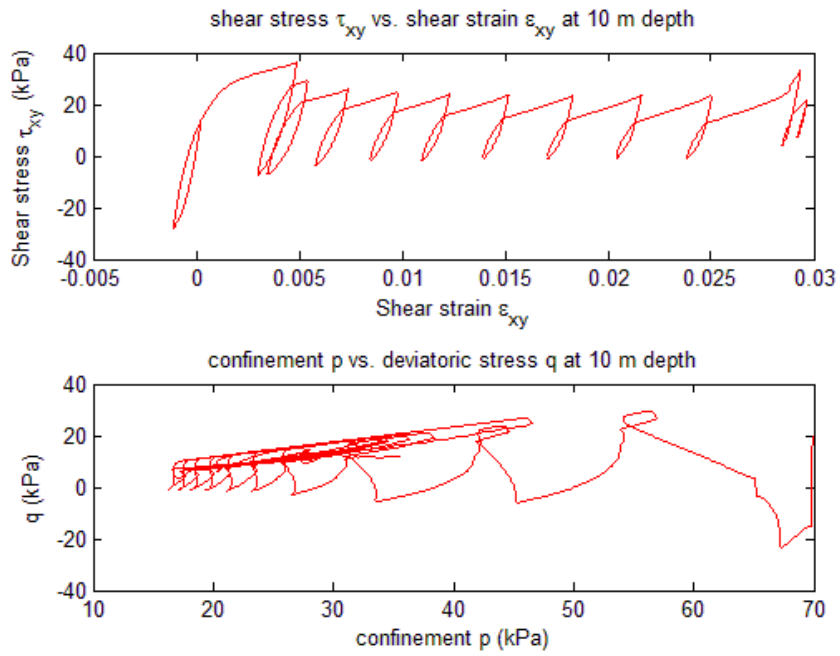


**Figure 51: Stress-strain output at 10 m depth.**

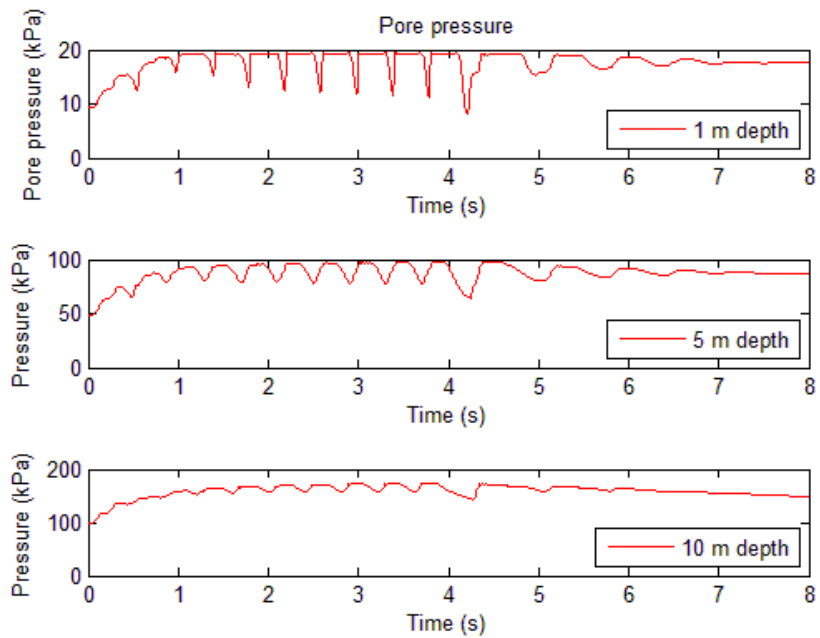


**Figure 52: Excess pore water pressure for soil element at different depth.**

## 6.2 Discussion

The UCSD soil model developed in OpenSees is useful in helping researchers get familiar with geotechnical system modeling in OpenSees. However, it is still under development and has some limitations in simulating nonlinear soil behavior, let alone the simulation coupling with structure. One of the limitations is the loading condition UCSD model can treat is limited. Another limitation is that that numerous parameters need to be predefined or selected with caution and other information needs to be incorporated where possible for a specific initial state of soil. However, in Cubrinovski and Ishihara's model, various combinations of initial void ratio and confining stress can be incorporated into state index, in other words, the formulation of this model is versatile for a general loading condition. Moreover, the state index  $I_s$  is integrated with the modified elasto-plastic into a single framework, and is embedded into other parameters in the way that only one set of values can be used to capture the prominent features of the sand behavior for any relative initial state. Therefore, the future work is to develop the nonlinear soil modeling based on Cubrinovski's stress-strain-dilatancy model in OpenSees and to conduct further simulations coupling with base isolated structure as well as to verify with implementation in other software or with the empirical testing.

## 7. Conclusions

Through implementation of Wolf's high dimensional model, a linear soil model coupled with a base-isolated three story structure is built.

The soil-structure interaction and base isolation effects are evaluated in this project based on the responses from lots of numerical simulations. The eigenvalue analysis of the system matrix gives the evidence that the soil structure interaction lengthens the periods of the structure.

The relationship between the system responses with respect to the hysteretic frictional force is plain to see. The base isolation system with large hysteretic frictional force is less effective in isolation. It couples the structure above it too tightly, which results in less deformation in base isolator and larger roof acceleration than anticipated. Moreover, the base isolation system with large hysteretic frictional force produces larger residual displacements for both base isolator and other floors.

On the other hand, the relationship between the system response with respect to the shear wave velocity in the range of 50 m/s to 200 m/s seems to be more randomly. This implies that the impact factor of shear wave velocity to the stiffness of soil is more difficult to assess. Therefore, nonlinear liquefied soil model is recommended to be calibrated for soil structure interaction evaluation in comparison with empirical testing.

## References

- Abe, M., Fujino, Y. and Yoshida, J. (2000). "Dynamic behavior and seismic performance of base-isolated bridges in observed seismic records", Proceedings of 12th World Conference on Earthquake Engineering, Paper No. 0321.
- Aubry, D., Hujeux, J. C., Lassoudiere, F. and Meimon, Y. (1982). "A double memory model with multiple mechanisms for cyclic soil behavior", International Symposium on Numerical Models in Geomechanics, Zurich.
- Asher, J.W., et al. (1995). "Seismic performance of the base isolated USC University hospital in the 1994 Northridge Earthquake", Seminar 1 on Isolation, Energy Dissipation and Control of Vibration of Structures, Santiago, Chile.
- Bouckovalas, G., Stamatopoulos, C.A. and Whitman, R.V. (1991). "Analysis of seismic settlements and pore pressures in centrifuge tests", ASCE Journal of Geotechnical Engineering Division 117: 1492-1508.
- Building Seismic Safety Council. (2003). NEHRP Recommended Provisions for Seismic Regulations for New Buildings and Other Structures, Part1: Provisions, FEMA 368, Federal Emergency Management Agency, Washington, D.C.
- Celebi, E., et al. (2012). "Non-linear finite element analysis for prediction of seismic response of buildings considering soil-structure interaction", Natural Hazards and Earth System Sciences, Vol.12 (11): 3495-3505.
- Celebi, M. (1996). "Radiation damping observed from seismic responses of buildings", Proceedings of 12th World Conference on Earthquake Engineering, Auckland, New Zealand.
- Celebi, M. (1996). "Successful performance of a based-isolated hospital building during the 17 January 1994 Northridge Earthquake", The Structural Design of Tall Building, Vol.5:95-109.
- Center for Earthquake Engineering Simulation  
<https://www.nees.rpi.edu/equipment/centrifuge/>
- Cubrinovski, M. and Ishihara, K. (1998). "Modelling of sand behavior based on state concept", Soils and Foundations, Vol.38 (No.3): 115-127.

- Cubrinovski, M. and Ishihara, K. (1998). "State concept and modified elastoplasticity for sand modeling", *Soils and Foundations*, Vol.38 (No.4): 213-225.
- Dafalias, Y. F. (1994). "Overview of constitutive models used in Velacs", *Verification of Numerical Procedures for the Analysis of Soil Liquefaction Problems*, Vol.2: 1293-1303.
- Elgamal, A., et al. (2002). "Computational modeling of cyclic mobility and post-liquefaction site response", *Soil Dynamics and Earthquake Engineering*, Vol. 22(4): 259-271.
- Elgamal, A., et al. (2003). "Modeling of cyclic mobility in saturated cohesionless soils", *International Journal of Plasticity*, Vol.19 (6): 883-905.
- Finn, W.D.L, Lee, K.W. and Martin, G.R. (1977). "An effective stress model for liquefaction", *ASCE Journal of Geotechnical Engineering Division* 103:517-533.
- Gutierrez, M., Ishihara, K. and Towhata, I. (1993). "Model for the deformation of sand during rotation of principal stress directions", *Soils and Foundations*, Vol.33 (3): 105-117.
- Iai, S. (1993). "Micromechanical background to a strain space multiple mechanism model for sand", *Soils and Foundations* 33-1:102-117.
- Idriss, I.M. and Boulanger, R.W. (2008). *Soil liquefaction during earthquakes (EERI MNO-12)*, 235 p.
- Ishihara, K. (1993). "Liquefaction and flow failure during earthquakes", 33<sup>rd</sup> Rankine Lecture, *Geotechnique*, Vol.43, No.3, pp.351-415.
- Iwan, W.D. (1967). "On a class of models for the yielding behavior of continuous and composite systems", *Journal of Applied Mechanics-ASME* 34:612.
- Kasai K, et al. (2010). "Full-scale shake table tests of 5-story steel building with various dampers", *Proceedings of 7th International Conference on Advances on Urban Earthquake Engineering*, Tokyo.
- Kelly, J. M. (1997). *Earthquake-Resistant Design with Rubber*, Second Edition, Springer-Verlag, London, England.
- Kelly, J. M. and Konstantinidis, D.A. (2011). *Mechanics of Rubber Bearings for Seismic and Vibration Isolation*, John Wiley and Sons, Chichester, England.

- Scruggs, J. T. and Gavin, H.P. (2010). Earthquake Response Control for Civil Structures. In Levine, W.S. (Ed.), Control System Applications, Second Edition (CRC PRESS).
- Maheshwari, B. K. and Sarkar, R. (2011). "Seismic behavior of soil-pile-structure interaction in liquefiable soils: parametric study", International Journal of Geomechanics, Vol.11 (4): 335-347.
- Matsuoka, H. and Sakakibara, K. (1987). "A constitutive model for sands and clays evaluating principal stress rotation", Soils and Foundations 27:73-88.
- Mazzoni, S., McKenna F., Scott, M.H., and Fenves, G.L. (2006). OpenSees command language manual, Pacific Earthquake Engineering Research Center.
- Mroz, Z. (1967). "On the description of anisotropic work hardening", Journal of Mechanics and Physics of Solids 15:612.
- Mylonakis, G. and Gazetas, G. (2000) "Seismic soil-structure interaction: Beneficial or detrimental?" Journal of Earthquake Engineering, Vol.4 (3): 277-301.
- Nagarajaiah, S. and Xiaohong, S. (2000). "Response of base-isolated USC hospital building in Northridge Earthquake", Journal of Structural Engineering, 126(10), 1177-1186.
- NEHRP recommended provisions for seismic regulations for new buildings and other structures (FEMA 450). Washington D.C.: National Institute of Building Sciences. 2004.
- Pande, G.N. and Sharma, K.C. (1983). "Multi-laminate model of clays-a numerical evaluation of the influence of rotation of the principal stress axes", International Journal for Numerical and Analytical Methods in Geomechanics 7:397-418.
- Prevost, J.H. (1978). "Plasticity theory for soil stress-strain behavior", Journal of Engineering Mechanics 104: 1177-1196.
- Proubet, J. (1991). "Application of computational geomechanics to description of soils behavior", Dissertation presented to the University of South California in partial fulfillment of the requirements for the degree of Doctor of Philosophy.
- Roscoe, K.H., Schofield, A.N. and Thurairajah, A. (1963). "Yielding of clays in states wetter than critical", Geotechnique, Vol.13, No.3: 211-240.

- Seed, H.B. (1979). "Soil liquefaction and cyclic mobility evaluation for level ground during earthquakes", *ASCE Journal of Geotechnical Engineering* 105:201-255.
- Skinner, R.I., Robinson, W.H and McVerry, G.H. (1993). *An introduction to seismic Isolation*, John Wiley and Sons, Chichester, England.
- Smith, I.M. (1994). "An overview of numerical procedures used in the VELACS project", *Proceedings of the International Conference. On Verification of Numerical Procedures for the Analysis of Soil Liquefaction Problems*, Davis, California, Arulanandan, K. And Scott, R.F. (eds.), Vol.2, pp.1321-1338.
- Towhata, I., Sasaki, Y., Tokida, K.I., Matsumoto, H., Tamari, Y. and Yamada, K. (1992). "Prediction of permanent displacement of liquefied ground by means of minimum energy principle", *Soils and Foundations* 32:97-116
- UC Davis NEES Center for Geotechnical Modeling  
<http://nees.ucdavis.edu/centrifuge.php>
- Wang, Z.L, Dafalias, Y.F. And Shen, C.K. (1990). "Bounding surface hypoplasticity model for sand", *Journal of Engineering Mechanics-ASCE*.116:983-1001.
- Wolf, J. P. (1985). *Dynamic Soil-Structure Interaction*. Prentice-Hall, Inc., Englewood Cliffs, New Jersey
- Wolf, J. P. (1994). *Foundation Vibration Analysis Using Simple Physical Models*, Prentice-Hall, Englewood Cliffs.
- Yang, Z. H., et al. (2003). "Computational model for cyclic mobility and associated shear deformation", *Journal of Geotechnical and Geoenvironmental Engineering* 129(12): 1119-1127.
- Yogachandran, C. (1991). "Numerical and centrifugal modeling of seismically induced flow failures", *Dissertation presented to the University of California at Davis, Dept. Of Civil Engineering in partial fulfillment of the requirements for the degree of Doctor of Philosophy*.
- Youd, T. L. and Idriss, I.M. (2001). "Liquefaction resistance of soils: Summary report from the 1996 NCEER and 1998 NCEER/NSF workshops on evaluation of liquefaction resistance of soils", *Journal of Geotechnical and Geoenvironmental Engineering*, Vol.127 (4): 297-313.

- Zaicenco, A. and Alkaz, V. (2007). "Soil-structure interaction effects on an instrumented building", *Bulletin of Earthquake Engineering*, Vol.5 (4): 533-547.
- Zaicenco, A. and Alkaz, V. (2008). "Analysis of the SSI from an instrumented building response", *Structural Design of Tall and Special Buildings*, Vol.17 (2): 387-399.
- Zienkiewicz, O.C. and Chang, C.T. (1978). "Nonlinear seismic response and liquefaction", *International Journal of Numerical and Analytical Methods in Geomechanics* 2: 381-404.
- Zienkiewicz, O.C. and Mroz, Z. (1984). "Generalized plasticity formulation and application to geomechanics", *Mechanics of Engineering Materials*, pp.665-679, Wiley.